Université d'Ottawa • University of Ottawa

Université d'Ottawa · University of Ottawa

FACULTÉ DES ÉTUDES SUPÉRIEURES ET POSTDOCTORALES

FACULTY OF GRADUATE AND POSTDOCTORAL STUDIES

Jamie Leigh RAMSEY
AUTEUR DE LA THÈSE - AUTHOR OF THESIS

M. Sc. (Physics)
GRADE - DEGREE

Department of Physics
FACULTÉ, ÉCOLE, DÉPARTEMENT - FACULTY, SCHOOL, DEPARTMENT

TITRE DE LA THÈSE - TITLE OF THE THESIS

The Optical Characterization of $In_yGa_{1-y}As_{1-x}N_x$

R. Williams
DIRECTEUR DE LA THÈSE - THESIS SUPERVISOR

CO-DIRECTEUR DE LA THÈSE - THESIS CO-SUPERVISOR

EXAMINATEURS DE LA THÈSE - THESIS EXAMINERS

E. Fortin

I. Calder

H. Mes

J.-M. De Koninck, Ph.D.
LE DOYEN DE LA FACULTÉ DES ÉTUDES SUPÉRIEURES ET POSTDOCTORALES

SIGNATURE

DEAN OF THE FACULTY OF GRADUATE AND POSTDOCTORAL STUDIES

The Optical Characterization of $In_yGa_{1-y}As_{1-x}N_x$

Jamie Leigh Ramsey

Thesis submitted to the
Faculty of Graduate and Postdoctoral Studies
in partial fulfillment of the requirements
for the degree of Master of Science in Physics

Department of Physics
University of Ottawa
Ottawa-Carleton Institute for Physics

© Jamie Leigh Ramsey, Ottawa, Canada, 2003

National Library of Canada

Bibliothèque nationale du Canada

Acquisitions and Bibliographic Services

Acquisisitons et services bibliographiques

395 Wellington Street
Ottawa ON K1A 0N4
Canada

395, rue Wellington
Ottawa ON K1A 0N4
Canada

Your file Votre référence
ISBN: 0-612-89908-X
Our file Notre référence
ISBN: 0-612-89908-X

The author has granted a non-exclusive licence allowing the National Library of Canada to reproduce, loan, distribute or sell copies of this thesis in microform, paper or electronic formats.

L'auteur a accordé une licence non exclusive permettant à la Bibliothèque nationale du Canada de reproduire, prêter, distribuer ou vendre des copies de cette thèse sous la forme de microfiche/film, de reproduction sur papier ou sur format électronique.

The author retains ownership of the copyright in this thesis. Neither the thesis nor substantial extracts from it may be printed or otherwise reproduced without the author's permission.

L'auteur conserve la propriété du droit d'auteur qui protège cette thèse. Ni la thèse ni des extraits substantiels de celle-ci ne doivent être imprimés ou aturement reproduits sans son autorisation.

In compliance with the Canadian Privacy Act some supporting forms may have been removed from this dissertation.

Conformément à la loi canadienne sur la protection de la vie privée, quelques formulaires secondaires ont été enlevés de ce manuscrit.

While these forms may be included in the document page count, their removal does not represent any loss of content from the dissertation.

Bien que ces formulaires aient inclus dans la pagination, il n'y aura aucun contenu manquant.

Canadä

Abstract

The dilute Nitride materials, InGaAsN, are studied as promising candidates for optical devices in the telecommunications wavelength range between 1.3 and 1.55μm. Such materials can be grown lattice matched to a GaAs substrate and could remove the need to work with structures based on the InGaAsP/InP materials, which are expensive and have poor temperature performance.

There are three main growth techniques for InGaAsN materials, chemical beam epitaxy (CBE), molecular beam epitaxy (MBE), and metal organic chemical vapour deposition (MOCVD). Of these three, MBE and MOCVD are used to grow the structures discussed in this thesis. X-ray diffraction and photoluminescence measurements are used for characterization. X-ray diffraction measurements provide the nitrogen concentration in the material, while photoluminescence measurements give the bandgap energy. The combination of these two results are then compared to the results from a band anti-crossing model that predicts the bandgap energy as a function of Nitrogen concentration. In addition, absorption and photoluminescence excitation measurements are used to investigate the Stokes shift in GaAsN material likely to have large composition non-uniformities.

To illustrate the progress made with InGaAsN material growth, processing and characterisation, a broad area laser structure is demonstrated that emits around 1.3μm.

Acknowledgments

I would to thank Dr. Robin Williams for all his help and for putting up with me for the past two years. It has been a long road and I would not have made it this far without him. I would also like to thank Dr. James Gupta and Dr. Zbig Wasilewski for the growth of the MBE samples and for being patient when I could not get results back to them in a timely manner. Thanks to Dr. Geof Aers for all the theory and for answering my questions when I didn't understand. For the MOCVD samples, my thanks go to Dr. Julian Noad and Dave Coulas from the CRC. As for everyone else working on the InGaNAs project they have my thanks as well. I would also like to thank Dr. Sylvain Raymond for helping me in taking the PLE measurements.

My parents: where would I be without them? This is for you. I could not have made it this far without your unquestioning faith in me. There are also the people that I shared my office with, Devika and Karine as well.

Statement of Originality

The work that is presented in this thesis is primarily the work of the author during her Masters research project under the supervision of Dr. Robin Williams. Work that was completed by her includes the following:

1. Photoluminescence measurements and interpretation of results on GaAsN and InGaAsN samples.
2. Sample preparation in the form of rapid thermal annealing, and sample cleaning.
3. Photoluminescence excitation measurements and Ti-Sapphire laser calibration.
4. Some X-ray measurements and fitting.

Samples for this work were provided by Drs. J. Gupta and Z. Wasilewski of the National Research Council and Dr. J. Noad and D. Coulas of the Communication Research Center. Dr. Geoff Aers of the National Research Council provided the theory for the Band anti-crossing model. Dr. James Gupta provided some of the X-ray data that was used in this research as well as performing some of the sample preparation.

The above work has led to the following papers

1. J.A. Gupta, P.J Barrios, G.C. Ares, R.L. Williams, J. Ramsey, Z.R Wasilewski, "Properties of 1.3 m InGaNAs laser material grown by MBE using N2/Ar RF plasma", Solid-State Electronics **46** (2003) 399-405.

2. J.A. Gupta, Z.R Wasilewski, B.J. Riel, J. Ramsey, G.C. Ares, R.L. Williams, G. I Sproule, A. Perovic, D. D. Perovic, T. Garanzotis, A. J. SpringThorpe, "Compositional control in molecular beam epitaxy of $GaAs_{1-x}N_x$ on GaAs (0 0 1) using an N2/Ar RF plasma", J. Cryst. Growth **242** (2001) 141-154.

3. J-Y. Duboz, J.A. Gupta, Z.R Wasilewski, J. Ramsey, B.J. Riel, R.L. Williams, G. I Sproule, "Band-gap energy of $In_xGa_{1-x}N_yAs_{1-y}$ as a function of N Content", Phys Rev. B **66** (2002)

This work has been presented at the following conferences

1. J. Ramsey, R.L. Williams, G.C. Aers, J.A. Gupta, J. Noad and D. Coulas, "A Photoluminescence Investigation of $GaAs_{1-x}N_x$ Alloys Grown by Metalorganic Vapor Phase Epitaxy: Effects of Rapid Thermal Annealing", Poster presentation at the Canadian Association of Physicists, Victoria, B.C. (2001)

2. J. Ramsey, R.L. Williams, G.C. Aers, J.A. Gupta, J. Noad and D. Coulas, "Effect of Rapid Thermal Annealing on MOCVD $GaAs_{1-x}N_x$ Alloys" Poster presentation at the tenth Canadian Semiconductor Technologies Conference, Ottawa, Ontario (2001)

3. J. L.Ramsey, R.L. Williams, S. Raymond, G.C. Aers, J.A. Gupta, Z. Wasilewski, B.J. Riel, J. Noad, D. Coulas, M. Adamcyk, and T. Tiedje, "A comparative study of the optical properties of $In_xGa_{1-x}N_yAs_{1-y}$ grown by MOVPE and MBE" Oral presentation at Photonics North, Quebec, Quebec, (2002)

Table of Contents

Abstract i

Acknowledgements ii

Statement of Originality iii

Table of Contents v

Chapter 1: Introduction 1

1.1 The Dilute Nitrides 2

1.2 Sample Growth 4
- 1.2.1 Molecular Beam Epitaxy (MBE)
- 1.2.2 Metal Organic Chemical Vapor Deposition (MOCVD)

Chapter 2: Theory 10

2.1 III-V semiconductors 11

2.2 Strain 13

2.3 Band Anti-Crossing model 14

2.4 Effective Mass 16

2.5 Strain Calculation in Dilute Nitrides 17

Chapter 3: Experimental Techniques 20

3.1 Photoluminescence 21
- 3.1.1 Recombination Pathways
- 3.1.2 Experimental arrangement for Photoluminescence
- 3.1.3 Fourier Transform Infra-red Spectroscopy
- 3.1.4 Cryogenic Equipment

3.2 Photoluminescence Excitation 26
3.2.1 Experimental arrangement for PLE

3.3 Absorption Measurements 28

3.4 Rapid Thermal Annealing 29

3.5 Double Crystal X-Ray Diffraction 30

Chapter 4: GaAsN 33

4.1 MOCVD GaAsN 34
4.1.1 Single Wells
4.1.2 Multiple Quantum Wells
Structural Measurements
Optical Studies
Annealing Experiments
(i) Experiments vs Anneal Time
(ii) Experiments vs Anneal Temperature
4.1.3 Absorption Measurements of GaAsN grown by MOVCD
4.1.4 PLE measurements of MOCVD grown GaAsN

4.2 MBE GaAsN 54
4.2.1 Single Wells
4.2.2 PLE measurements of MBE grown GaAsN

4.3 Conclusions 62

Chapter 5: InGaNAs 64

5.1 MOCVD InGaAsN 65

5.2 MBE InGaNAs 69
5.2.1 Wafer Mapping
X-ray Results
Photoluminescence Measurements
(i) Integrated Intensities
(ii) Emission Energies

5.3 Annealing of InGaNAs 77

5.4 Temperature Dependent Measurements 80

5.5 Conclusion 84

Chapter 6: InGaNAs Laser Material 87

6.1 Introduction 88

6.2 Laser and Test Structure Design 88

6.3 Optical Characterization 90

6.4 Laser Tests 91

6.5 Conclusions 93

Chapter 7: Conclusions and Future work 96

Chapter 1

Introduction

This chapter gives a general introduction to the InGaAsN materials system and describes the molecular beam epitaxy and metal organic chemical vapor deposition techniques that were used to prepare the samples investigated for this thesis.

1.1 The Dilute Nitrides

In contrast to what might be expected when alloying GaAs (bandgap ~ 1.5eV) with GaN (bandgap ~ 3.5eV), the bandgap of dilute alloys of GaAsN ([N] ~ 1%) is actually substantially lower than that of GaAs. A diagram of the bandgap energy as a function of lattice constant for typical III-V alloys is shown in Fig 1.1 below.

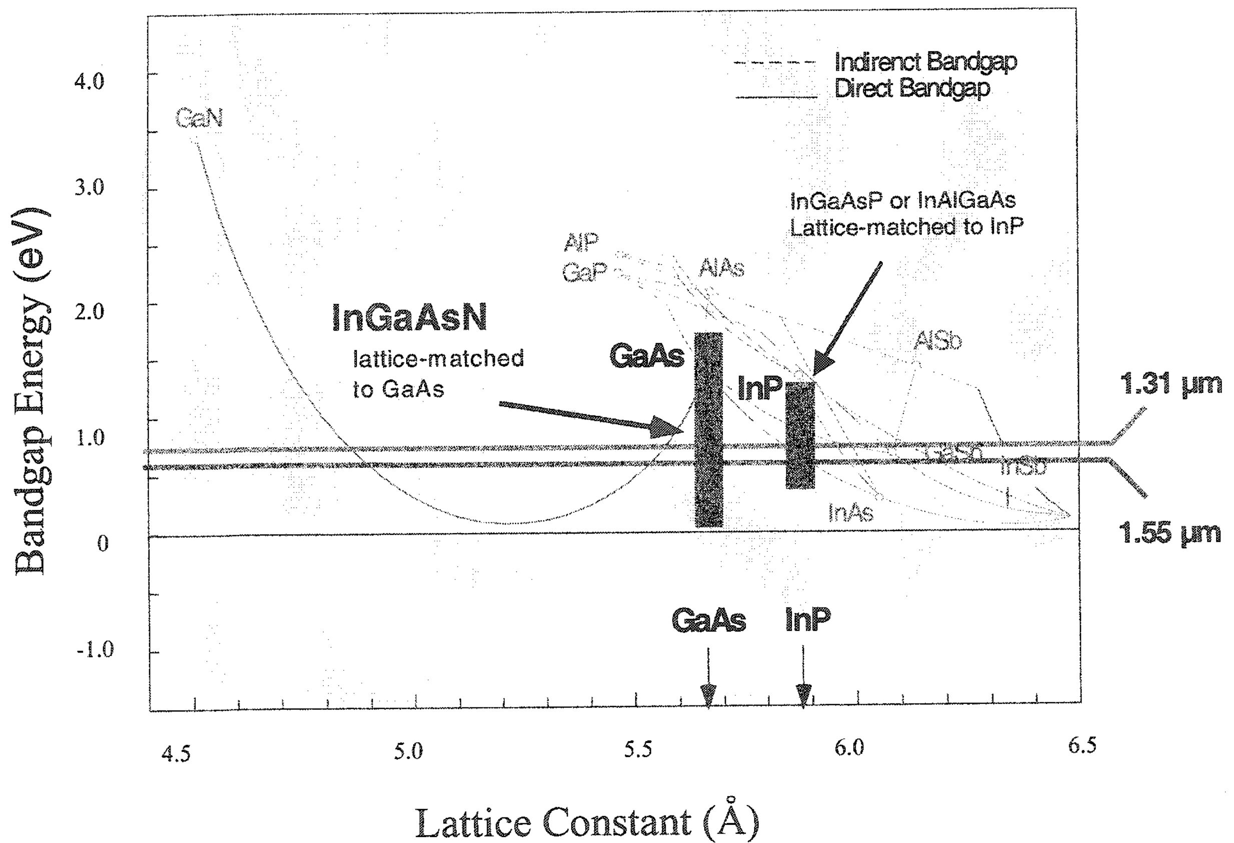

Fig. 1.1: Variation of bandgap with lattice parameter for a number of III-V semiconductor materials.

Bandgap 'bowing' in mixed III-V semiconductor alloys is typically parameterised using a formula of the type,

$$\Delta E_g(x) = b.x(x-1)$$

where 'b' is a bowing parameter which is usually a fraction of an electron volt. For dilute GaAsN, where the As and N atoms are significantly different in size and chemical behaviour, the bowing parameter is of the order of 20eV and is strongly dependent upon the chemical composition [1,2,3]. This large bowing parameter indicates a strong reduction in the semiconductor bandgap for low nitrogen concentrations and has stimulated interest in the GaAsN materials system for telecommunications applications around $\lambda=1.3$ and $\lambda=1.55\mu m$. At present, the majority of telecommunications devices in this wavelength region make use of the InGaAsP materials system which can be grown lattice matched on an InP substrate. This materials system suffers from a number of drawbacks however, including high cost of the substrate material and poor temperature performance because of low band offsets. The InGaAsN materials system, which can be grown lattice-matched to cheaper GaAs substrates, is therefore seen as an interesting alternative to span the region between 1.3 and 1.55μm.

For emission around 1.3μm, one of the most promising technologies for high speed fiber optic communications is the InGaAsN Vertical Cavity Surface Emitting Laser (VCSEL) [4,5,6], in which quantum wells of laser gain material are sandwiched between highly reflecting multi-layer Bragg mirrors. The technology for these Bragg mirrors is highly developed for the GaAs/AlGaAs materials system, where devices operating around 850nm have been used extensively for local area networks, but is considerably more difficult if InGaAsP must be used. Hence, using InGaAsN grown on GaAs substrates, companies are pushing to sell cheap 1.3μm VCSELs using GaAs/AlGaAs Bragg technology.

InGaAsN material is also being studied for applications in satellite-based solar cells. In such applications, it is of paramount importance to reduce the total mass that must be carried into orbit, so that even a few percent increase in the efficiency of solar cell material can produce millions of dollars in savings. Because of the reduced bandgap, InGaAsN solar cells are expected to reach efficiencies as high as 40% of the theoretical maximum and should challenge the presently used Si (23%) and InGaP/GaAs (30%) devices.

InGaAsN material has also been suggested as a candidate for high-speed electronic devices and indeed, this was one of the major reasons for the introduction of the dilute nitrides project at the NRC and for the interest of Nortel Networks [7]. GaAs-based heterojunction bipolar transistors (HBTs) are used in 10Gb/sec electronic systems, but have been challenged by improving Si/SiGe and InP/InGaAs devices, which operate at lower voltages and therefore require less power. By using InGaAsN in the base layer of a GaAs HBT, it is hoped that the operating voltage can be reduced, so that the usefulness of the GaAs-based devices can be prolonged.

1.2 Sample Growth

1.2.1 Molecular Beam Epitaxy (MBE)

Molecular Beam Epitaxy or MBE is the most popular III-V semiconductor growth technique for materials grown in a research environment. A schematic illustration of a typical MBE reactor that might be used in the growth of nitride materials is shown in Fig 1.2.

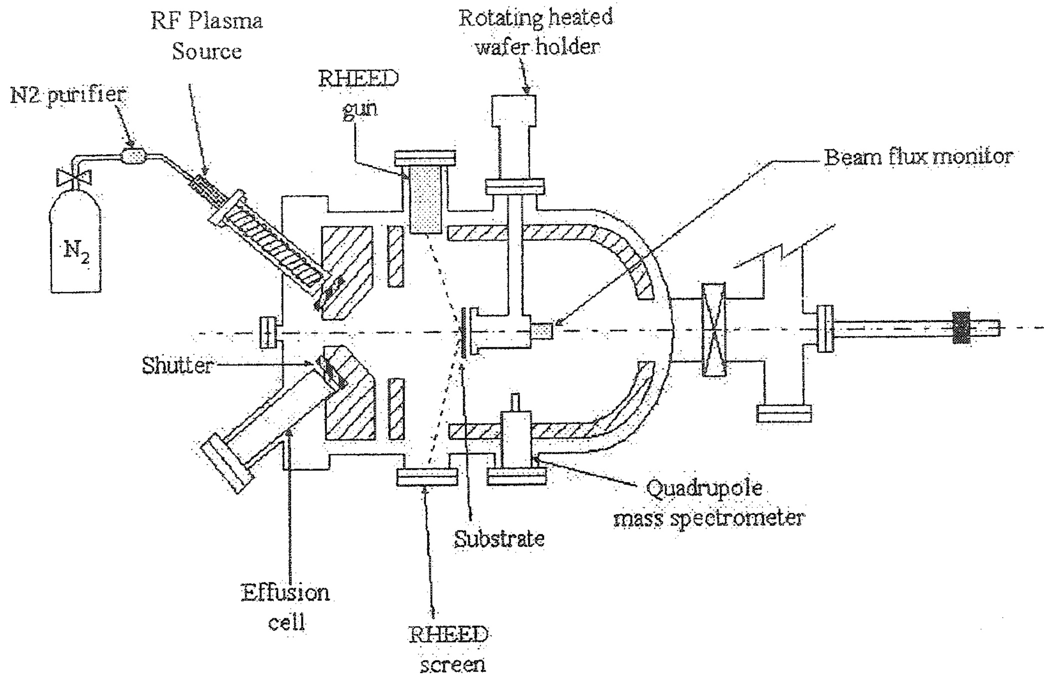

Fig. 1.2: Schematic Illustration of a typical Molecular Beam Epitaxy growth chamber used in the growth of dilute Nitride materials (courtesy of University of Boston, Department of Electrical and Computer Engineering).

MBE systems typically consist of three separate chambers isolated one from another by vacuum valves. The first chamber allows wafers to be transferred from outside into the MBE system without breaking the main vacuum. Once the wafer is transferred into this first chamber, sometimes called the entry lock, the chamber is pumped, normally with a turbo-molecular pump, and a valve is opened to allow transfer of the wafer into a 'preparation' chamber. In this preparation chamber, the substrate wafer is prepared for epitaxial growth by heating to outgas surface contaminants such as water vapor. Depending upon the type of growth to be performed and the actual materials being used, other surface preparation techniques, such as ion bombardment for example, may also be employed.

Once the substrate wafer is ready, it is transferred from the preparation chamber into a growth chamber such as that shown in Fig 1.2. The growth chamber, and also the rest of the MBE system, is constructed from stainless steel. The growth chamber is designed to hold a vacuum of approximately $1\text{-}5\times10^{-11}$mbar and is pumped by a combination of high throughput vacuum pumps such as large turbo-molecular pumps, ion pumps and He cryo-pumps. The stainless steel chamber is also designed to enclose a nitrogen cryo-shroud, which allows continuous circulation of liquid nitrogen around the inside of the chamber. This cryo-shroud acts as an efficient pump for residual gas, as stray gas molecules condense out onto it.

Inside the growth chamber, the sample is mounted onto a heated, rotating holder, where it is rotated in the molecular beams from a series of effusion cell sources. Depending on the materials system to be grown, these sources will include such materials as gallium, indium, aluminum, arsenic, silicon (n-dopant) and beryllium (p-dopant). To produce a flux from each cell, the cells are held at elevated temperatures, whilst to stop the flux a remote controlled shutter can be placed in front of each source.

For the MBE grown InGaAsN materials discussed in this thesis, a modified VG V80H system was used. Indium and gallium were supplied from thermal effusion cells as described above, arsenic was supplied in the form of As_2 molecules by pre-cracking the normally emitted As_4 molecules and active nitrogen was supplied by an Applied EPI Unibulb^{TM} radio frequency (RF) plasma source operating with a mixture of N_2 and argon [8]. The substrate temperature was typically 450°C during growth of nitrogen containing layers, but was higher, typically 620°C, for the growth of GaAs.

As suggested in the schematic of Fig 1.2, the MBE system used for the samples discussed here, was also equipped with a number of in-situ monitoring tools, including a mass spectrometer for residual gas analysis and a reflection high energy electron diffraction (RHEED) system for monitoring the reconstruction of the wafer surface.

1.2.2 Metal Organic Chemical Vapor Deposition (MOCVD)

Metal organic chemical vapor deposition (MOCVD) is the industrial method of choice for growing both III-V and II-VI semiconductor materials. A schematic of a typical system is shown in Fig 1.3.

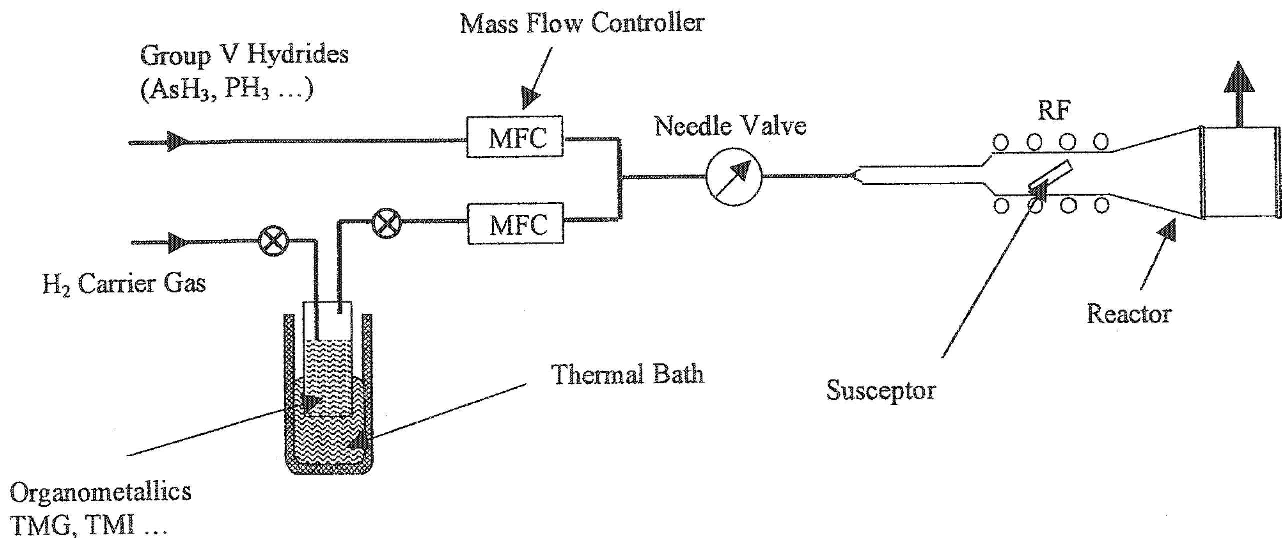

Fig. 1.3: Schematic illustration of a typical Metal Organic Chemical Vapor Deposition (MOCVD) system.

The precursors used in typical III-V MOCVD growth include the group V hydrides such as arsine (AsH_3) and phosphine (PH_3) which are supplied in the form of gases and the group III organometallic materials such as Trimethylgallium (TMG) and Trimethylindium (TMI) which are taken up during the passage of carrier gases, such as

hydrogen, through liquid bubblers. The flow of each precursor material is carefully metered using precision mass flow controllers before the reagents are mixed and then passed into the growth chamber. In addition to the precursors mentioned above, 1-1-dimethylhydrazine (DMHy) and Tertiarybutylarsine were used at the communications research center (CRC) as sources of nitrogen and arsenic respectively for the MOCVD InGaAsN materials discussed in this thesis.

The MOCVD reactor itself is particularly simple and consists of a double walled quartz tube through which the reagents are passed, whilst maintaining, in our case, a moderately low pressure of 200mbar. The thoroughly cleaned and outgassed semiconductor substrate is placed at an angle on a graphite susceptor, which is heated using an inductively coupled RF coil wrapped around the quartz chamber.

References

[1] Su-Huai Wei and Alex Zunger, PRL 76 664 (1996).

[2] M. Kondow, K. Uomi, K. Hosomi, and T. Mozume, Jpn. J. Appl. Phys. 33, L1056 (1992).

[3] M. Weyers, M. Sato, and H. Ando, Jpn. J. Appl. Phys. 31, L853 (1992).

[4] M. C. Larson, M. Kondow, T. Kitatani, K. Nakahara, K. Tamra, H. Inoue, and K. Uomi, IEEE Photonics Technol. Lett. 10, 188 (1998).

[5] C. W. Coldren, M. C. Larson, S. G. Spruytte, and J. S. Harris, Electron. Lett. 36, 951 (2000).

[6] C. Ellmers, F. Höhnsdorf, J. Koch, C. Agert, S. Leu, D. Karaiskaj, M. Hofmann, W. Stolz, and W. W. Rühle, Appl. Phys. Lett. 74, 2271 (1999).

[7] R. McKinnon, NRC Internal Technical Report (2001).

[8] J.A.Gupta, Z.R.Wasilewski, B.J.Riel, J.Ramsey, G.C.Aers, R.L.Williams, G.I.Sproule, A.Perovic, D.D.Perovic, T.Garanzotis, A.J.SpringThorpe, Journal of Crystal Growth 242 (2002) 141–154

Chapter 2

Theory

This chapter gives a brief introduction to the bandstructure and optical properties of direct gap III-V semiconductors and introduces the concept of strained layer materials that is of considerable importance for dilute nitride materials. The band anti-crossing model that is used to understand the bandstructure of the dilute nitrides is also discussed.

2.1 III-V semiconductors

Because of their direct bandgap, the III-V semiconductors have gained considerable importance in modern optical devices. To understand the operation of these devices it is necessary to understand the bandstructure of III-V materials close to the band edge. A schematic diagram of the bandstructure of a III-V material close to the band edge is given below in Fig 2.1. At the zone centre, the conduction band edge has s-like

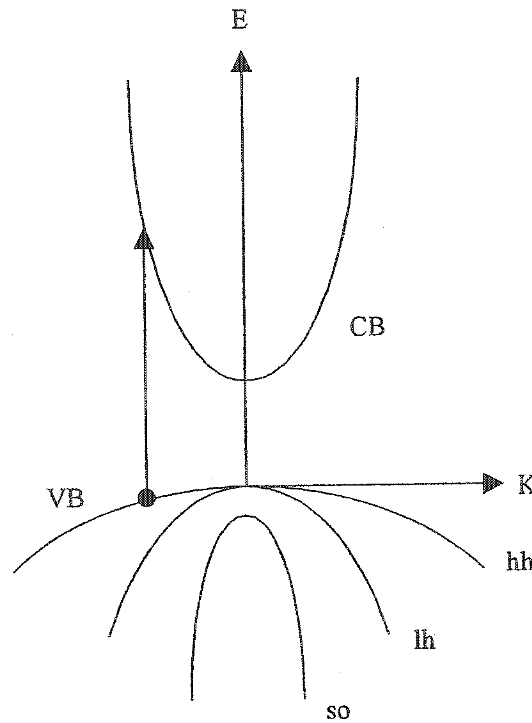

Fig. 2.1 Schematic illustration of the near band-edge dispersion in III-V materials.

character, whilst the valence band edge has p-like character, consisting of three, doubly spin degenerate levels. These represent heavy holes ($j = 3/2$, $m_j = \pm 3/2$), light holes ($j = 3/2$, $m_j = \pm 1/2$) and spin-orbit split off holes ($j = 1/2$, $m_j = \pm 1/2$). For III-V materials of

cubic symmetry, the heavy and light hole states are degenerate at the zone centre, whilst the spin-orbit split off level is depressed somewhat because of the relativistic spin-orbit interaction [1]. Away from the zone centre, the eigenstates are mixed and in principle have contributions from all three valence band levels, as well as the conduction band and higher lying levels. In equilibrium, the valence band states are all full and the conduction band states are empty.

Inter-band optical transitions on a diagram such as Fig 2.1 are generally drawn as vertical arrows between occupied levels in the valence band and empty levels in the conduction band, ignoring any linear momentum associated with the optical photon. This view of the optical transition process is a single particle picture and leads to a prediction for optical absorption in the near edge region that has a square root dependence on the energy above the band edge. In many situations of practical interest this square root dependence is not observed and the single particle picture of optical absorption is very far from adequate.

The inter-band optical absorption process is really a two-particle process. In addition to the electron appearing in the conduction band, a hole is left in the valence band. The electron and hole have opposite charge and can interact via their mutual Coulomb attraction, to generate a set of discreet "hydrogenic" bound levels below the energy gap. The optical absorption rate for the interacting electron and hole can be calculated from a two-particle Schrodinger equation, factored to separate relative and centre of mass motion, in much the same way as the hydrogen atom [2,3].

2.2 Strain

Over the last 20 years, numerous optical devices have been employed which make use of strained, heteroepitaxial films. A good example of this is the use of InGaAs quantum well active layers during the growth of GaAs/AlGaAs lasers. For GaAs active layers, the conduction and valence band curvatures around the zone centre, and therefore the density of states, are very unequal. In a laser structure this asymmetry in the density of states between conduction and valence bands leads to a higher than necessary threshold current density, since states are filled in the valence band during pumping that cannot be accessed with k-conserving transitions from the conduction band. This limitation was overcome by the use of strained quantum well active regions.

The lattice constant of unstrained, bulk InGaAs is larger than that of GaAs, so that if a thin layer of InGaAs is deposited on a GaAs substrate, the InGaAs lattice must distort if it is to be commensurate with the substrate. In this case, a biaxial compression of the InGaAs is required in the plane of the interface, which is accompanied by a uniaxial extension of the lattice along the growth direction, perpendicular to the plane. This tetragonal distortion of the InGaAs lattice has been found to proceed in a manner that does not produce unwanted defects, such as threading dislocations, provided that the thickness of the strained layer is kept below some critical thickness [4].

Because of the breaking of the cubic symmetry of the lattice introduced by tetragonal distortion, the degeneracy of the heavy and light-hole valence bands is lifted in strained III-V materials. Under the influence of biaxial compression, the valence band becomes heavy-hole-like along the growth direction, and light-hole-like in the plane, producing a density of states that more closely resembles the conduction band.

2.3 Band Anti-Crossing model

The addition of nitrogen to GaAs and InGaAs produces additional complications to those discussed above for strained materials systems. Although the addition of nitrogen to GaAs produces a strain in the normal way (this time a biaxial tension when grown on GaAs) and the valence band energy configuration responds in the normal way, additional effects occur in the conduction band [5]. These additional effects include a larger than expected electron mass, a strong bowing of the bandgap as a function of nitrogen concentration and the observation of a new, resonant level within the GaAs conduction band [4]. These effects have been described using a model which includes the presence of a strongly localised nitrogen level within the GaAs conduction band and its resulting interaction with the delocalised GaAs conduction band states. The model, first postulated by Shan and co-workers, has come to be known as the band anti-crossing model and in its simplest form can be represented by the following 2x2 Hamiltonian [6-10],

$$\hat{H} = \begin{pmatrix} E_N & V \\ V & E_C \end{pmatrix}$$

Where E_N is the nitrogen concentration dependent energy of the localised level, V is the nitrogen concentration dependent interaction energy and E_c is the non-parabolic GaAs conduction band energy that can be parameterised via the following dispersion relation

$$\frac{\hbar^2 k^2}{2m_0^*} = E_C\left(1 + \alpha E_C\right)$$

Where m* is the effective mass and α=0.61eV^{-1} is the non-parabolicity parameter. Using these values as input, we arrive at a phenomenological conduction band dispersion for GaAsN that is shown in Fig 2.2 below,

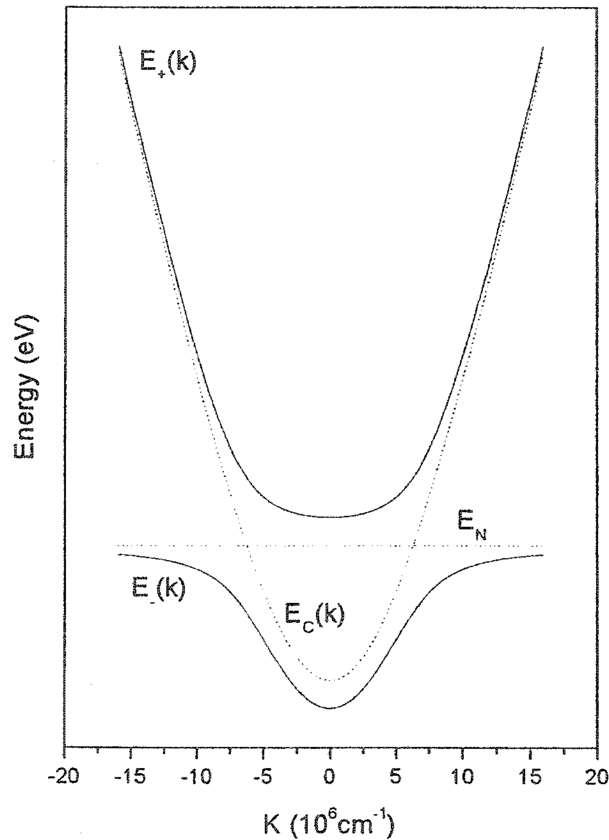

Figure 2.2 Band anti-crossing model used in the conduction band of InGaAsN materials.

As seen in the graph above, the original GaAs conduction band is split into two separate bands by the presence of the localised nitrogen level. The dashed parabolic line is the original GaAs band, whilst the dotted straight line is the nitrogen level that is added in the presence of nitrogen. The solid lines are the two levels that are created when these two bands combine. Using this band anti-crossing model, combined with the usual effects

of pseudomorphic strain, a model can be generated to explain the band edge shifts observed due to the addition of nitrogen [8,11,12]. Dr. Geof Aers at the NRC has generated such a model to explain the shifts discussed in this thesis.

2.4 Effective Mass

If we assume that we have a parabolic conduction band, we can calculate the effective mass by simply inverting the dispersion relation:

$$E = \frac{\hbar^2 k^2}{2m^*}$$

As discussed above however, this is not the case. Instead we must use a definition for the effective mass that is valid for non-parabolic bands:

$$\frac{1}{m^*} = \frac{1}{\hbar^2 \mathrm{k}}\left|\frac{\partial E}{\partial k}\right|$$

Using this definition we arrive at an expression for the effective mass within the band anti-crossing model as

$$\frac{1}{\mathrm{m}_{\pm}^*} = \frac{1}{2\mathrm{m}_0^*}\frac{1}{(1+2\alpha \mathrm{E_C})}\left\{1 \pm \frac{(\mathrm{E_C} - \mathrm{E_N})}{\sqrt{(\mathrm{E_C} - \mathrm{E_N})^2 + 4\mathrm{V}^2}}\right\} \qquad \text{eqn. 2.4.1}$$

An example of the calculated effective mass is given in fig 2.3 for the same parameters used in fig 2.2. The effect of the interacting nitrogen level is seen to be an increase in the band edge effective mass for the E. level, due to the repulsion between bands and the corresponding 'flattening' of the dispersion [13].

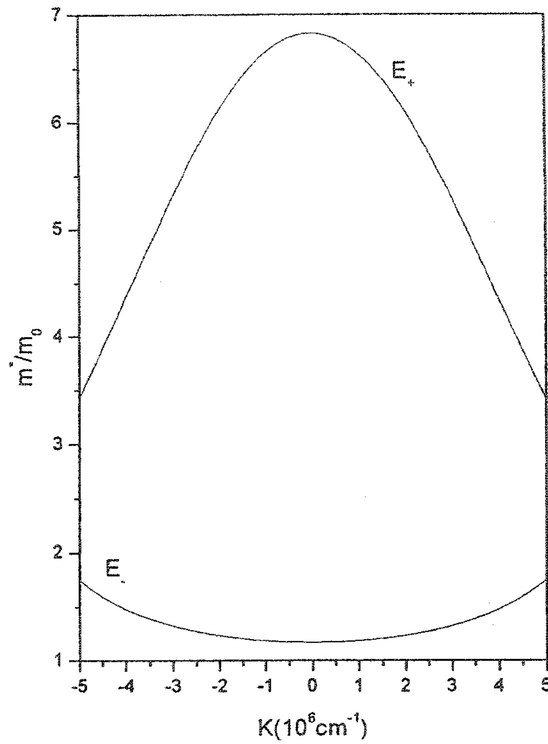

Figure 2.3: Effective mass in the band anti-crossing model calculated using equation 2.4.1 for the same parameters used in fig 2.2.

2.5 Strain Calculation in Dilute Nitrides

Including all of the effects discussed above, Dr. Aers has produced a model for the InGaAsN bandgap for material pseudomorphicaly strained to a GaAs substrate. The results of the calculation can be seen in Fig 2.4 below.

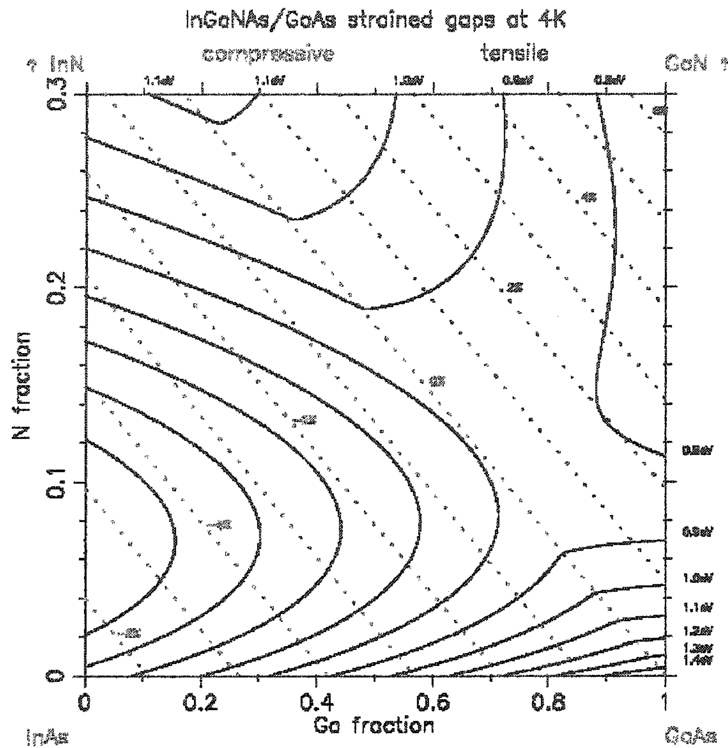

Figure 2.4: Energy gap of InGaAsN alloys strained to a GaAs substrate for a sample temperature of 4K.

The diagram is split into two regions, showing tensile (blue) and compressive (green) strain, by the line of lattice match (red) for which [In]≈2.84[N]. In the compressive region of the diagram, optical transitions occur between heavy hole and conduction band levels, whilst in the tensile region transitions occur between the light hole and conduction band. For nitrogen containing material grown without any Indium content the resulting strain is tensile, whilst the addition of Indium can bring the system back to lattice match. With the type of information afforded by fig 2.4, it is possible to tailor the bandgap of the material in a variety of ways.

References

[1] J. R. Chelikowski, and M. L. Cohen, Phys. Rev. B 14, 556 (1976).

[2] C. Weisbuch, and B. Vinter, *Quantum Semiconductor Structures: Fundamentals and Applications* (Academic Press, San Diego, 1991).

[3] J. H. Davies, *The physics of low-dimensional semiconductors* (Cambridge University Press, Cambridge, 1997).

[4] I. Vurgaftman, J. R. Meyer, and L. R. Ram-Mohan, J. of App. Phys. 89, 5815 (2001).

[5] Yong Zhang, A. Mascarenhas, H. P. Xin, and C.W. Tu, Phys. Rev. B 61, 4433 (2000).

[6] R. J. Potter, N. Balkan, X. Marie, C. Carrer, E. Bedel, and G. Lacoste, Phys. Stat. Sol, 187, 623 (2001).

[7] A. Lindsay, and E. P. O'Reilly, Solid State Communications 112 443 (1999).

[8] J. D. Perkins, A. Mascarenhas, Yong Zhang, J. F. Geisz, D. J. Friedman J. M. Olson, and Sarah R. Kurtz, Phys. Rev. Lett. 82, 3312 (1999).

[9] W. Shan, W. Walukiewicz, J. W. Ager III, E. E. Haller, J. F. Geisz, D. J. Friedman J. M. Olson, and S. R. Kurtz, Phy. Rev. Lett. 82, 1221 (1999).

[10] A. Al-Yacoub and L. Bellaiche, Phys. Rev. B 62, 10 847 (2000).

[11] Yong Zhang, A. Mascarenhas, H. P. Xin, and C. W.Tu, Phys. Rev. B. 61, 7479 (2000).

[12] P. J. Klar, H. Gruning, J. Koch, S. Schafer, K. Volz, W. Stolz, W. Heimbrodt, A. M. Kamal, A. Lindsay, and E. P. O'Reilly, Phys. Rev. B 64 (2001).

[13] C. Skierbiszewski, P. Perlin, P. Wisnieski, W. Knap, T. Suski, W. Walukiewicz, W. Shan, K. M. Yu, J. W. Ager, E. E. Haller, J. F. Geisz, and J. M. Olson, Appl. Phys Lett. 76 2409 (2000).

Chapter 3

Experimental Techniques

In this chapter I will describe the experimental apparatus that was used to characterize the InGaAsN material system. The main technique that was employed was photoluminescence, but both absorption and photoluminescence excitation experiments were attempted. Double crystal x-ray diffraction was used to examine the quality of the InGaAsN crystal structure and to determine nitrogen concentrations and layer widths.

3.1 Photoluminescence

Photoluminescence (PL) is a radiative process in which the material under investigation is probed using a coherent beam of light that has a photon energy larger than the material bandgap ($h\nu > E_g$). In the simplest form of the experiment, the incident photon creates an electron hole pair which, after thermalisation, recombine to emit a photon. From the quantum mechanical selection rules, if an electron is in the conduction band and is allowed to recombine with a hole in the valence band, there will be a photon emitted with the equivalent energy of the bandgap that is being probed. Fig. 3.1 below shows a schematic of the recombination process in a typical III-V semiconductor material [1-4].

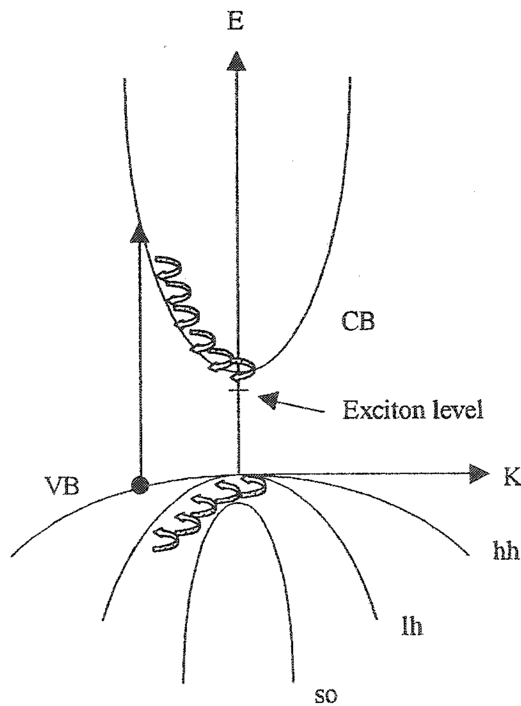

Fig. 3.1: Band diagram of a typical III-V semiconductor. Carrier thermalisation after absorption of a photon is shown by curved arrows.

3.1.1 Recombination Pathways

As discussed in chapter 2, the emission from high quality, direct gap, III-V semiconductors is usually excitonic in origin, arising from the annihilation of an electron-hole pair bound together by their mutual Coulomb interaction. In certain circumstances, the binding energy of an exciton can be further enhanced by the presence of a crystal defect or impurity. Under these circumstances, the exciton will become trapped around the defect to produce a bound exciton. Binding centres for the exciton can include neutral and ionised impurites acting as either donors or acceptors. Such bound exciton luminescence will then include neutral donor bound excitons (D^o,X), neutral acceptor bound excitons (A^o,X), ionised donor bound excitons (D^+,X) and ionised acceptor bound excitons (A^-,X). The emission energy for a bound exciton is slightly less than that for a free exciton and the energy difference is characteristic of the impurity and can be used as a valuable tool in identifying the impurities present in high quality material [1-4].

In addition to the excitonic recombination pathways discussed above, other transition mechanisms are possible such as the donor-acceptor pair (DAP) transition which involves the annihilation of a mobile electron and hole trapped around a closely spaced donor-acceptor pair, or the free-to-bound transitions, (e, A^0) and (h, D^0), which involve the recombination of free electrons (holes) with neutral acceptors (donors). For much of the GaAs-based material discussed in this thesis, these types of transition are prevalent, resulting in strong luminescence peaks around 1490meV [1-4].

3.1.2 Experimental arrangement for Photoluminescence

Figure 3.2 below shows a schematic illustration of the experimental arrangement that was used to investigate the photoluminescence produced by the InGaAsN samples. The sample under investigation was held on a sample probe inserted into the sample space of a liquide helium bath cryostat. Details of the system are given below.

Luminescence was excited using a variety of visible laser sources including HeNe (632.8nm), Argon-ion (488nm, 514nm) and a frequency doubled Nd:YVO_4 (532nm). The excitation beam was directed to the sample using a sequence of simple mirrors and a two-lens beam expander that allowed control of the laser spot size on the sample. A 2"x 2" dichroic beamsplitter was used in the collection path to allow direction of the visible excitation beam and simultaneous transmission of the photoluminescence signal in the near infra-red.

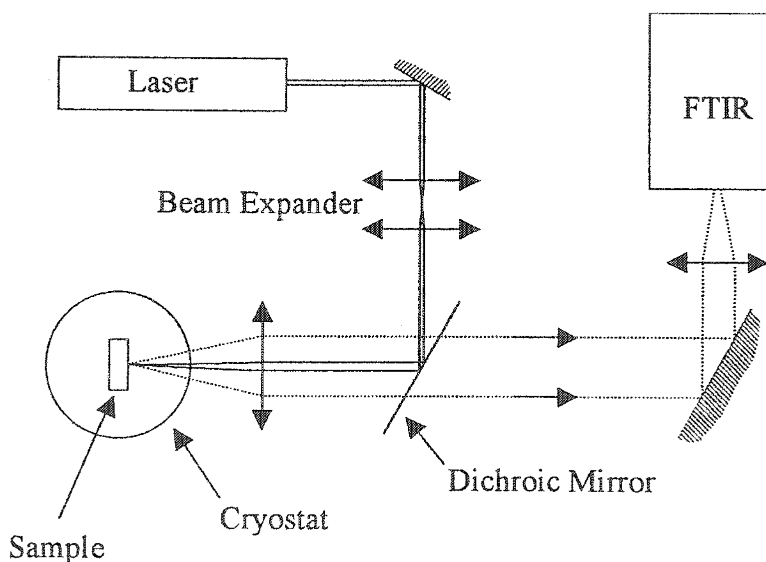

Fig. 3.2: Schematic of the experimental arrangement used to collect photoluminescence from InGaAsN samples held at 4K.

Luminescence from the sample was collected using the same objective lens used for excitation and then imaged onto the cooled InGaAs detector of a Bomem MB-160 Fourier transform infrared (FTIR) spectrometer. Experimental spectra were collected by a personal computer using Bomem Grams_32 software.

3.1.3 Fourier Transform Infra-red Spectroscopy

An FTIR spectrometer can be thought of as a simple Michelson interferometer:

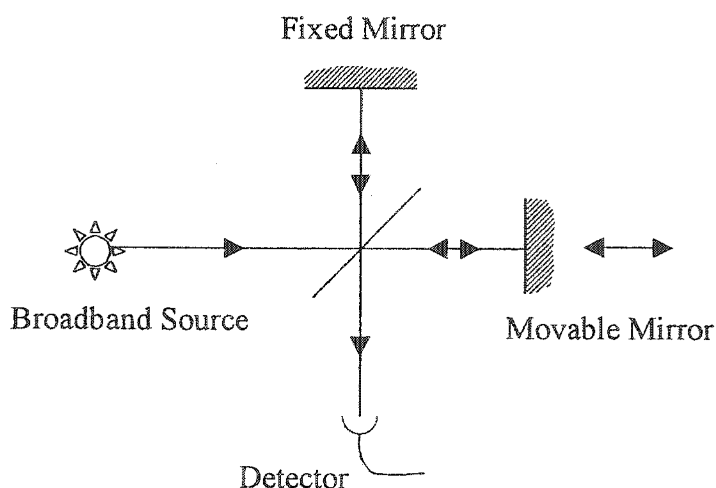

Fig. 3.3: Fourier Transform Infrared Spectroscopy

Emission from the sample is represented by the broadband source; it contains many wavelengths simultaneously. On entering the spectrometer, the light of interest is split into two spatially separate paths by a 50:50 beam splitter. Mirrors in both paths are used to retro-reflect the light back onto the beam splitter, where it is re-combined and directed to a single element detector. One of the retro-reflecting mirrors can be scanned to produce a path difference between the two beam paths, so that the detector measures

an interference signal as a function of this path difference that is recorded as an interferogram. Once this interferogram is stored, fast Fourier transform techniques are used to invert the data and produce a spectrum of intensity vs. wavelength for the broadband source.

FTIR spectroscopy is a useful way to make spectroscopic measurements because it can be done in real time. Data is collected simultaneously for all wavelengths present in the source. Signal throughput to the detector is also large and is not reduced by the requirements of large ruling density and small slit-width experienced in high resolution, grating-based spectroscopy.

3.1.4 Cryogenic Equipment

The liquid helium bath cryostat that was used in our experiments is shown below in Fig 3.4. The cryostat consists of concentric chambers used to store the liquid cryogens, helium and nitrogen. Each cryogen is separated from its neighbor and from the outside world by vacuum chambers. The sample under investigation is held in an evacuable sample space that can be connected to the liquid helium reservoir using an adjustable needle valve. The sample temperature was easily adjusted and controlled by balancing the rate of cooling from incoming helium with the rate of heating supplied by a resistive heater mounted directly on the sample probe. In this manner, the sample temperature could be continuously varied between approximately 4.3K and 300K. To ensure good thermal contact, whilst avoiding any inadvertent strain, the sample was attached to a copper heat sink using wound teflon tape.

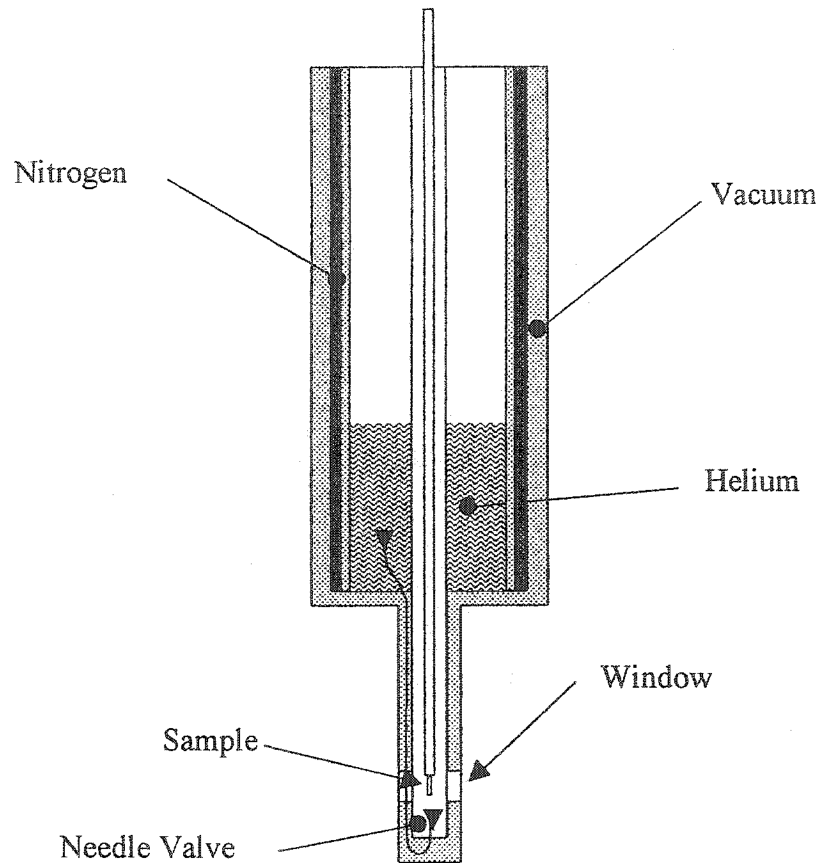

Fig. 3.4: Schematic illustration of the liquid helium bath cryostat used in photoluminescence experiments.

3.2 Photoluminescence Excitation

One of the major limitations of a photoluminescence experiment is that it frequently does not give access to information about the excited states of the system. Once carriers have been excited in the semiconductor, they very quickly thermalise to the ground state. Photoluminescence excitation (PLE) is an experiment designed to give access to the excited states [3]. In PLE, the detection energy is fixed on the low energy edge of the ground state emission, whilst the laser pump frequency for excitation is swept to higher energy. To a good approximation, this allows one to map out the density of

optically allowed transitions (DOS) for the semiconductor, although in principle this assumes that carriers can thermalise easily to the ground state with a rate that does not depend strongly on their generation position within the bandstucture.

3.2.1 Experimental arrangement for PLE

For PLE experiments, a frequency doubled Nd:YVO_4 laser was used as the pump source for a tunable Ti-Sapphire laser. The Ti-sapphire laser was able to emit over the wavelength region between 890nm and 1μm, suitable for a limited number of the GaAsN samples. The Ti-Sapphire laser was tuned using a birefringent filter within the laser cavity and the emission wavelength was calibrated as a function of the filter position (adjusted using a micrometer drive). This calibration was checked periodically to ensure accuracy of the data.

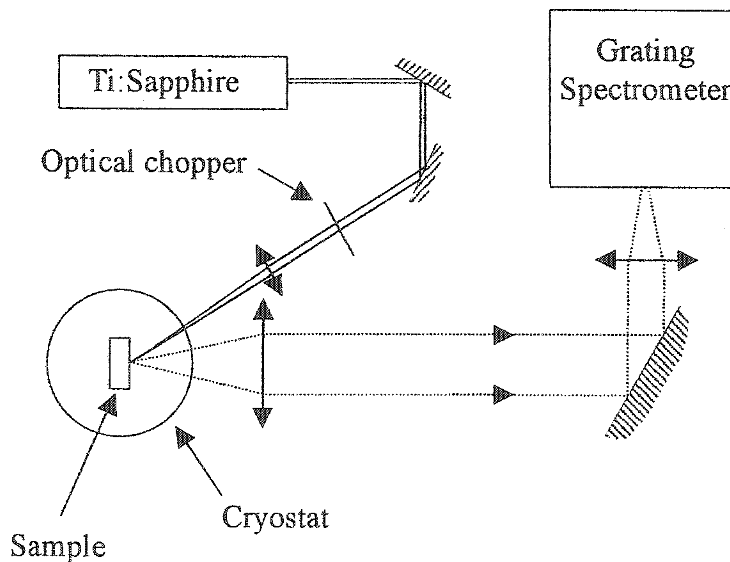

Fig. 3.5: Experimental arrangement used for PLE experiments. The Ti:Sapphire laser is pumped using the 532nm emission from a doubled Nd:YVO_4 laser (not shown).

A schematic illustration of the experimental arrangement used for PLE is shown in fig 3.5 above. The birefringent tuning element of the Ti:Sapphire laser was controlled by computer, so that a scan corresponded to moving the motor step by step and recording the signal detected by the Ge detector attached to the grating spectrometer. To account for any variations in the output power of the Ti:Sapphire laser as a function of emission wavelength, the output power was sampled using a beam splitter (not shown) and the recorded data scaled to the detected output power. To improve the signal to noise ratio, the incident laser was chopped at a frequency of 210Hz using an optical chopper and the output of the Ge detector was measured using phase sensitive detection.

Unlike the standard photoluminescence experiment described above, the pump radiation and the collected luminescence were separated in the PLE experiments by an angle of approximately 45 degrees. This was done to avoid the large amount of scattered light close to the detected energy. For similar reasons, a double grating spectrometer was used for dispersion to improve the rejection of stray light so that detection could be achieved closer to the pump energy.

3.3 Absorption Measurements

Absorption measurements are similar to PLE measurements in that they give information about the excited states of the system. For weakly absorbing samples, such as thin quantum wells for example, these experiments can be difficult however because they seek to measure a small change (the absorption) on top of a large signal (the transmitted light) [3]. In spite of this difficulty, a small number of absorption experiments were attempted using the FTIR apparatus described above. The experiments were done using a

broadband, white light source to irradiate the sample, which was placed directly in the FTIR interferometer, just in front of the detector. To account for absorption within the sample that does not come from the quantum well of interest, a control experiment was performed on a piece of substrate material placed next to the sample of interest. Once the substrate and the sample are measured, a ratio is taken and the absorption peak is observed.

Although the absorption experiments are in principle simpler than the PLE measurements, they suffer from low signal to noise if the level of absorption cannot be increased by using many quantum wells or by using multiple passes through the sample. If PLE measurements cannot be performed, because of lack of a broadband tunable source for example, then absorption measurements should be considered.

3.4 Rapid Thermal Annealing

In many of the experiments discussed here, the samples were treated, post growth, using a rapid thermal annealing technique. This was done to improve the luminescence properties of the as-grown material that was found, at least in the initial material produced, to be quite poor. The first step in the annealing process was the cleaning of the samples. Sample cleaning is important, both to avoid incorporation of contaminants into the sample during high temperature annealing and also to protect the cleanliness of the equipment itself. The samples were cleaned in a cleanroom environment by immersing them in a sequence of Trichloroethene, Acetone, and Isopropyl alcohol. Samples were placed in the trichloroethene for five minutes and then rinsed off with acetone to avoid contamination of the acetone bath. Similarly, samples were then placed in acetone for

five more minutes and then rinsed off with the isopropyl alcohol. A further five minutes was used for the isopropyl alcohol, before rinsing with distilled water and drying using nitrogen gas.

A Heatpulse 410 was used for annealing. Samples were placed on a silicon wafer and surrounded on all sides by a GaAs enclosure made from pieces of substrate. This enclosure was used to ensure that the surface of the sample was exposed to an arsenic rich environment during annealing (supplied by evaporation from the surrounding pieces of GaAs). Once the samples were placed on the Si wafer and the door of the annealing apparatus closed, a period of roughly five minutes was used in which purge gas (nitrogen) was circulated to remove any impurities from the ambient gas. With this done, the annealing proceeded under nitrogen gas. The range of temperatures employed was from 500^0C to 850^0C.

3.5 Double Crystal X-Ray Diffraction

High resolution, double crystal, X-ray diffraction was used to investigate the crystal structure of the InGaNAs samples [5]. With such measurements one can determine the thickness of constituent layers, whether or not the samples are fully strained and how much nitrogen and/or indium is present. The results of the x-ray diffraction measurements (detected intensity vs crystal angle) are called x-ray rocking curves.

A schematic illustration of the geometry of a single crystal x-ray diffraction experiment is given below in Fig 3.6. X-rays from a single frequency source, in our case Cu $K_{\alpha 1}$ radiation with a wavelength of approximately 1.54056Å, impinge on the target.

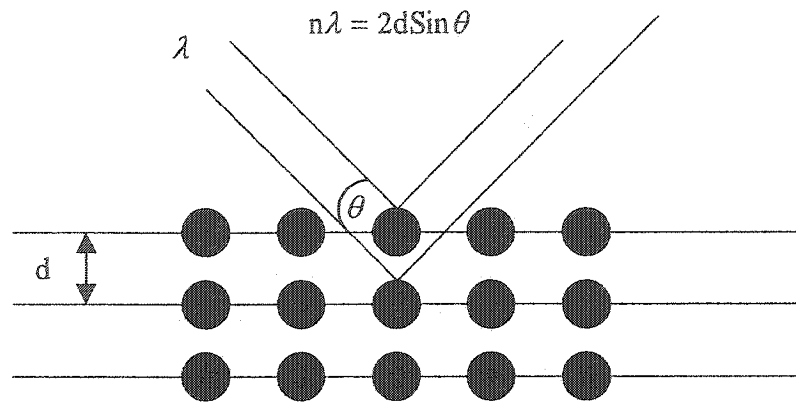

Fig. 3.6: Geometry for single crystal x-ray diffraction.

For constructive interference of the multiple x-ray wavelets scattered from the host atoms, the Bragg condition must be satisfied. As the crystal is rotated, the Bragg condition is fulfilled for a series of crystal planes, giving rise to the x-ray rocking curves observed. For the x-ray measurements reported here, a Philips MRD system using an asymmetric double-crystal, channel-cut monochrometer was used. Data were taken in a standard $\theta/2\theta$ arrangement (i.e. by moving the crystal through θ and the detector through 2θ) by scanning around the GaAs (004) substrate Bragg reflection. The resulting x-ray rocking curves were analysed using the BEDE Rads x-ray fitting procedures [6].

References

[1] M. Razeghi, The MOCVD challenge, (Bristol, Adam Hilger, 1989).

[2] S. Perkowitz Optical Characterization of Semiconductors: Infrared, Raman and Photoluminescence Spectroscopy, (Academic Press, London, 1993).

[3] J. I. Pankove *Optical Processes in Semiconductors,* (Dover Publication, NY, 1971).

[4] N. Peyghambarian, S. W. Kock, and A. Mysyrowicz, *Introduction to Semiconductor Optics,* (Prentice Hall, New Jersey 1993).

[5] R. L. Snyder, J. Fiala, H. J. Bunge *Defect and Microstructure Analysis by Diffraction (International Union of Crystallography Monographs on Crystallography, 10)*, (Oxford University Press, Oxford, 1999).

[6] BEDE Scientific, Inc. UK.

Chapter 4

GaAsN

This chapter describes the optical characterisation of GaAsN material grown by both MOCVD and by MBE. Characterisation of the dilute nitrides was begun using this ternary material instead of the full InGaAsN in an attempt to understand the incorporation of nitrogen, without the added complication of an Indium content to consider. The main results of this chapter are photoluminescence measurements, although double crystal x-ray measurements were used to confirm the structural quality of the samples and to determine the nitrogen concentration in the layers.

4.1 MOCVD GaAsN

4.1.1 Single Wells

Before beginning a study of GaAsN materials grown by MOCVD, GaAs samples grown in the same reactor were studied in photoluminescence. An example of luminescence obtained from an 8μm thick epilayer of GaAs grown at 650°C using Trimethyl Gallium (TMG) and Arsine as the source gases is shown in Fig. 4.1 below.

The luminescence signal observed is typical of high quality material grown using TMG as the source of Gallium [1]. Strong excitonic features are observed around the band edge whose energetic positions allow them to be identified as resulting from donor and

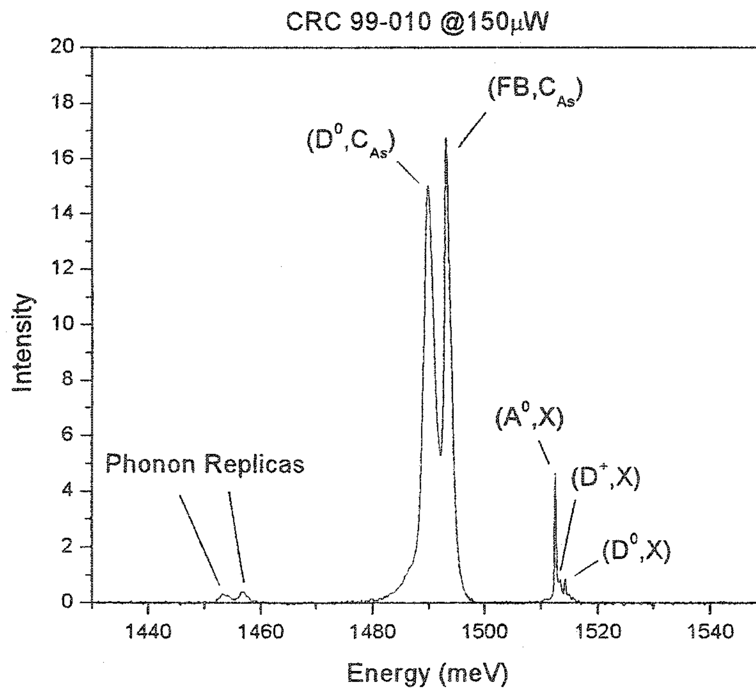

Fig. 4.1: Near band edge luminescence from a GaAs sample grown by MOCVD using Arsine. Excitonic features are observed around 1512meV, but the spectrum is dominated by free-to-bound and donor acceptor pair transitions related to Carbon around 1490meV.

acceptor-bound exciton complexes. Two strong luminescence bands around 1490meV dominate the spectrum however, which are related to transitions involving the inadvertent incorporation of Carbon impurities on Arsenic sites of the crystal. These transitions are highly localized and as such produce strong phonon sidebands that can be seen around 1455meV.

To facilitate the incorporation of nitrogen, it is necessary to lower the MOCVD growth temperature. The effect of this non-optimal growth temperature can be seen directly in luminescence from a second thick GaAs layer grown at 550°C, as shown in Fig. 4.2.

In this sample, the excitonic features observed previously at the band edge are completely absent, indicating a much poorer sample quality. Instead, the luminescence is dominated by the donor-acceptor pair transition at approximately 1490meV. A weak shoulder is also

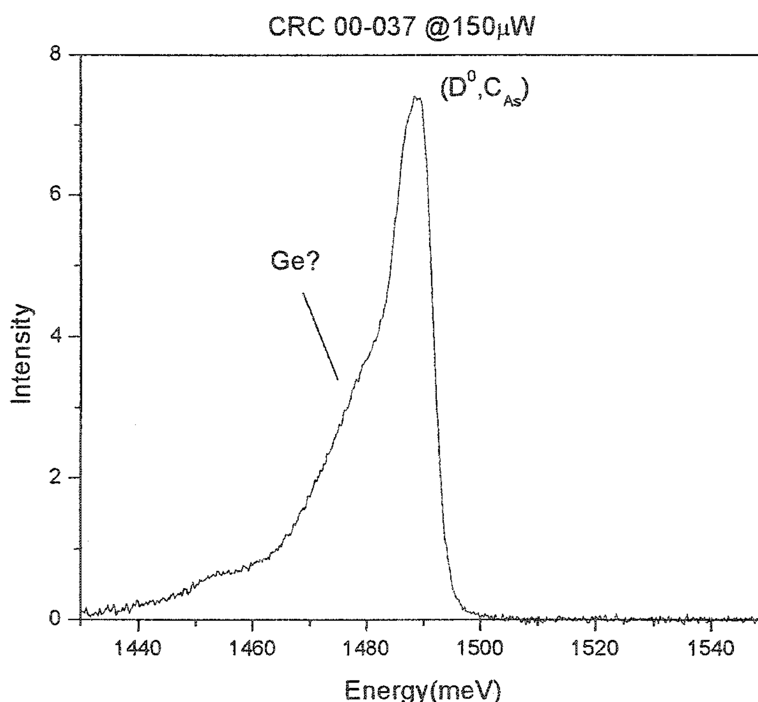

Fig. 4.2: Photoluminescence from an MOCVD GaAs epilayer grown at a substrate temperature of 550°C, using Arsine as the source gas. No excitonic band edge luminescence is observed. Instead the emission is dominated by a broad donor-aceptor pair transition.

seen around 1480meV, which may suggest other impurities in the MOCVD system, possibly Germanium.

Following the growth of these GaAs samples, a series of thick GaAsN layers, with 50nm thick ternary layers and a 5nm GaAs cap, were grown to investigate the effects of group V/ group III ratio on the optical properties of the material. The growth details of these samples are given in Table 4.1

Sample No.	TBA Flow (sccm)	DMHy Flow (sccm)	TMG Flow (sccm)	XRD θ (arcsecs)
00-019	25	25	5	420
00-020	25	50	5	690
00-021	25	75	5	1350
00-022	25	100	5	1825
00-023	37	25	5	280
00-024	37	50	5	480
00-025	37	75	5	713
00-026	37	100	5	1075
00-027	50	25	5	325
00-028	50	50	5	410
00-029	50	75	5	550
00-030	50	100	5	800
00-031	15	100	5	No peak
00-032	15	25	5	750
00-033	15	50	5	1750
00-034	15	75	5	2680

Table 4.1: Growth parameters for the GaAsN samples used to explore the effects of V/III ratio. All layers were grown at 520°C and consisted of a 50nm thick GaAsN and a 5nm GaAs cap layer grown on a GaAs substrate.

Photoluminescence spectra from this series of samples are shown below.

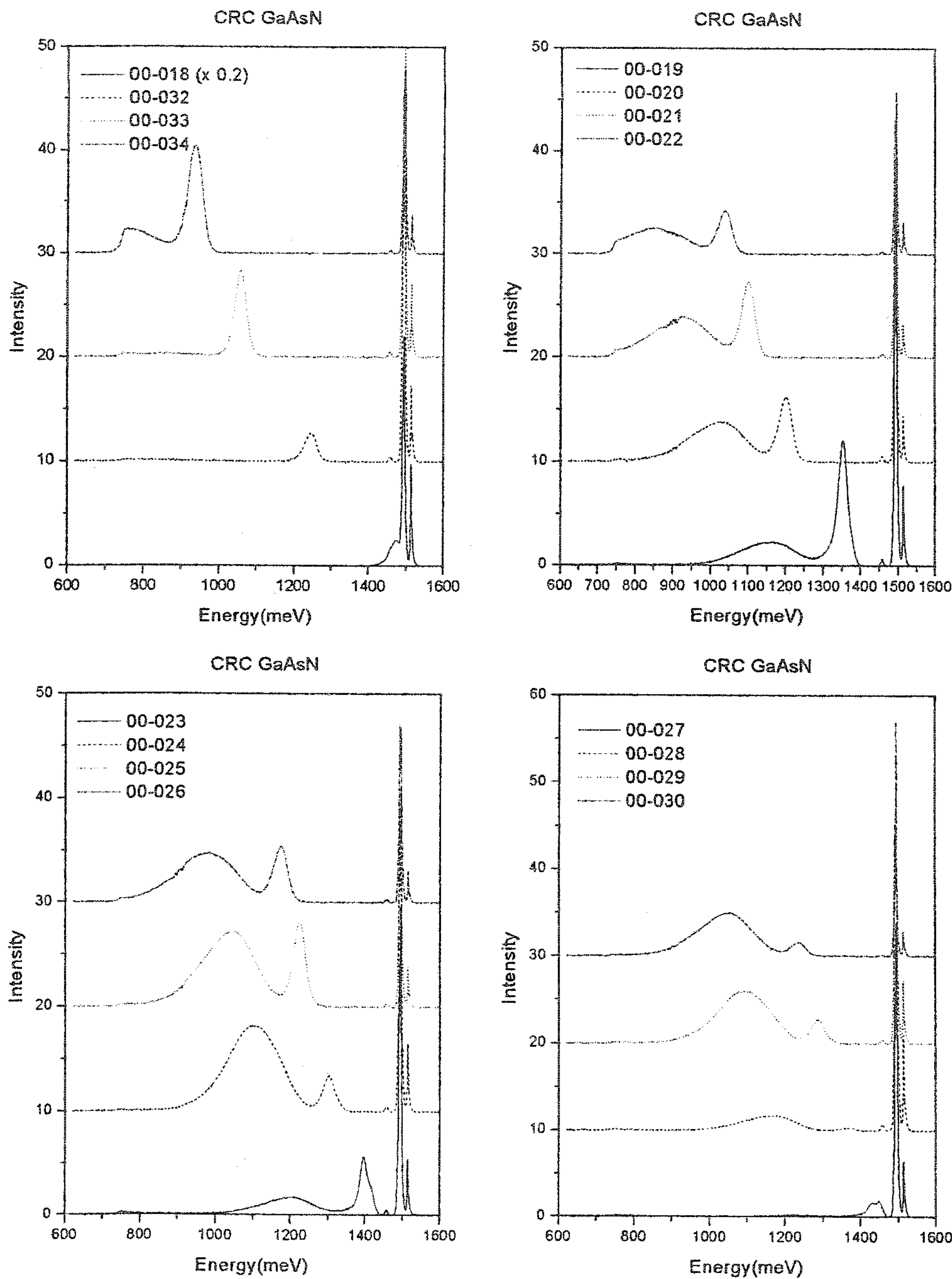

Fig 4.3: Photoluminescence data from a series of MOCVD GaAsN samples of varying V/III ratio and nitrogen composition. Details of the sample design are given in Table 4.1. Experiments were performed at 4.5K, with 4.7mW of HeNe excitation and a spot size of approximately 100μm. Detection was achieved at a resolution of $8cm^{-1}$ using 20 averaged scans from an FTIR and InGaAs detector.

Considering this data, it is clear that most samples show strong features around 1500meV related to emission from the GaAs cap layer, and possibly the substrate, with additional features at lower energy related to emission from GaAsN layers of varying composition. Sample 00-018 is a GaAs sample grown under the same conditions as the GaAsN samples, with a V/III ratio of 7:1. This GaAs sample shows clear band edge exciton features in addition to the Carbon related features around 1490meV. A deeper, defect related emission band centered at 1468meV is also observed.

Considering first the series of samples grown at a Tertiary Butyl Arsine (TBA) flow of 15 Sccm (Fig. 4.3, top left panel), we note first that no luminescence was observed from sample 00-031, corresponding to a Dimethyl Hydrazine (DMHy) flow of 100Sccm. This sample corresponds to a high nitrogen fraction in the gas phase and considering that no x-ray diffraction peak was visible, we conclude that the sample is of a particularly poor quality and unlikely to be of a high optical quality. For the remaining three samples, GaAsN related peaks are observed in the spectral region below1300meV, with a general trend towards lower emission energies with increasing nitrogen content (increasing DMHy flow) as expected. Samples 00-032 and 00-033 show single, long wavelength emission peaks, at energies of 1247meV and 1056meV respectively, whilst sample 00-034 shows a strong peak at 935meV and a second peak cut off by the detector response at 740meV. For the other samples, grown at high values of TBA flow, a similar two-peak emission characteristic is observed for the GaAsN layers, with again a general trend towards longer wavelength emission for larger DMHy flows at fixed TBA flow. For a given sample, the two-peak GaAsN emission characteristic is seen to correspond to a narrower peak at high energy and a broader peak at lower energy. It also seems clear that

increasing the TBA flow results in the broad peak at lower energy beginning to dominate the optical emission. As a function of increasing pump intensity (data not shown) it is found that the low energy peak begins to saturate and the higher energy peak begins to dominate. For this reason we identify the low energy peak as resulting from a limited number of defect states within the band gap of the GaAsN layer.

A summary of the optical data extracted from the photoluminescence, along with the nitrogen concentration in the solid extracted from x-ray data and the nitrogen fraction in the gas phase calculated as N_{frac}=DMHy(Sccm)/(DMHy(Sccm)+TBA(Sccm)) is presented in Table 4.2.

Sample No.	GaAsN (meV)	Xray (arcsecs)	N_{comp}	DMHy (Sccm)	TBA (Sccm)	N_{frac}
00-019	1351.5	420	0.00967	25	25	0.5
00-020	1202	690	0.01507	50	25	0.66667
00-021	1100	1350	0.02827	75	25	0.75
00-022	1036.9	1825	0.03777	100	25	0.8
00-023	1393.6	280	0.00687	25	37	0.40323
00-024	1300	480	0.01087	50	37	0.57471
00-025	1224.8	713	0.01553	75	37	0.66964
00-026	1172.2	1075	0.02277	100	37	0.72993
00-027	1429.5	325	0.00777	25	50	0.33333
00-028	1367.8	410	0.00947	50	50	0.5
00-029	1283.6	550	0.01227	75	50	0.6
00-030	1251.6	800	0.01727	100	50	0.66667
00-032	1245.4	750	0.01627	25	15	0.625
00-033	1056	1750	0.03627	50	15	0.76923
00-034	935.5	2680	0.05487	75	15	0.83333

Table 4.2: Sample characteristics extracted from photoluminescence measurements and x-ray diffraction data.

The x-ray data allows us to examine how the nitrogen is incorporated into the growing layer as a fraction of nitrogen in the gas phase. Figure 4.4 below shows that the nitrogen

incorporation is independent of the TBA flow and depends only upon the fraction of nitrogen in the gas phase [2,3,4]. However, it is clear from the photoluminescence data discussed above that the material quality is not independent of the TBA flow.

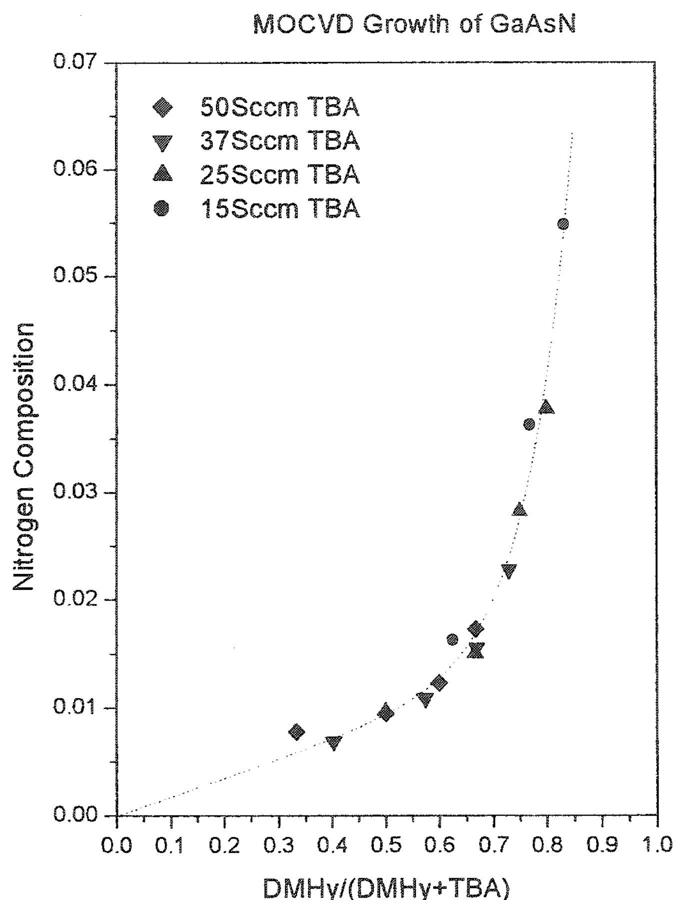

Fig. 4.4: Nitrogen concentration in the solid as a function of nitrogen concentration in the gas phase. The dotted line is a guide to the eye only.

From the x-ray and photoluminescence data, we can also extract the variation of GaAsN bandgap with nitrogen concentration for these thick well samples [5]. For such thick wells we are able to ignore any complications due to electron and hole confinement energies, which would require knowledge of the effective masses for us to interpret.

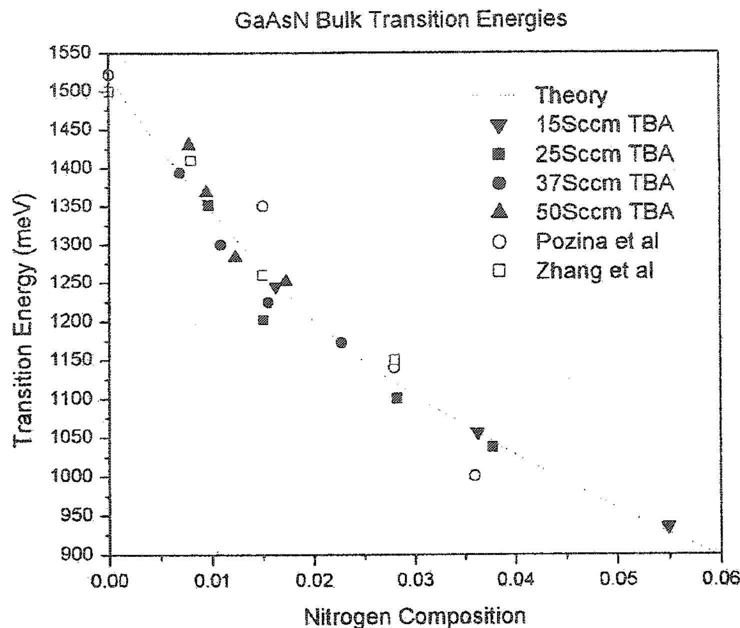

Fig. 4.5: Variation of GaAsN bandgap energy as a function of Nitrogen concentration for the thick single quantum well samples discussed in the text. Open squares and circles show comparative data from other groups.

Bandgap data as a function of nitrogen concentration is shown in Fig 4.5 above for the series of GaAsN samples grown by MOCVD. The bandgap varies between approximately 1515meV for bulk GaAs and 930meV for 5.5% GaAsN. The variation of bandgap with nitrogen concentration that we observe does not depend upon the TBA flow in any systematic way and is in good agreement with measurements made elsewhere by Pozina [6] and Zhang [7]. Based upon this data, a model was developed by Dr. G.C. Aers from NRC, taking into account composition and strain effects and also including the band anti-crossing mechanism that arises from nitrogen related defects which are resonant within the conduction band, as discussed in chapter 2. The predictions of this theory are shown as a dashed line in Fig 4.5.

4.1.2 Multiple Quantum Wells

Structural Measurements

Following on from the thick, single MOCVD GaAsN wells, a series of multiple quantum well (MQW) samples were grown and both their structural and optical properties were studied. Table 4.3 below gives the nominal growth parameters for these samples:

Sample No.	# of Periods	GaAs Width (nm)	GaAsN Width (nm)	% Nitrogen
00-056	10	10	7	1%
00-057	10	10	7	2%
00-058	10	10	7	3%
00-059	5	10	7	5%
00-060	10	10	7	4%
00-061	10	10	7	5%
00-062	10	10	7	2%

Table 4.3: Sample design for MOCVD GaAsN Multiple Quantum Wells

Each sample was grown at a substrate temperature of 520°C, with a TMG flow of 5Sccm and a TBA flow of 15Sccm, except for sample 00-062, which was grown with a TBA flow of 25Sccm.

Double Crystal X-Ray diffraction is an extremely useful technique for the investigation of structural quality in semiconductor materials. The results that can be derived from such measurements include the width of the constituent layers and the concentration of particular elements that have been added to a binary compound. In the case described here, we are interested in the ternary compound GaAsN, with changes in the nitrogen content from layer to layer. This makes the task of calculating the concentrations of the groups V elements particularly easy. The program that is used to fit the x-ray data is the BEDE Rads Mercury non-linear least-squares package [8].

Representative double crystal x-ray spectra taken on the MQW samples are shown below in Fig 4.6.

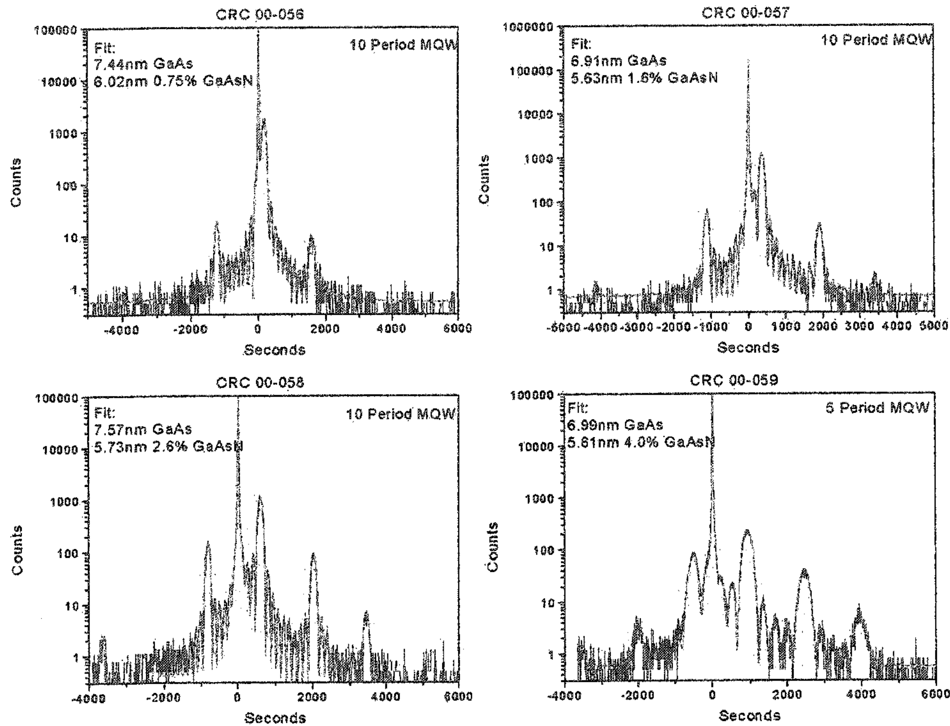

Fig. 4.6: Double crystal x-ray rocking curves from MOCVD GaAsN MQW samples, with fits obtained using the RADS Mercury software.

The very sharp peak that is observed close to 0 arc seconds is the main Bragg peak that comes from the GaAs substrate and epilayer. The first peak to the right of the substrate peak (+ve arc seconds) can be thought of as representing the average nitrogen composition within the multi-layer sample. As a function of increasing average nitrogen composition, this peak moves further away from the substrate peak. This trend is demonstrated clearly in the four x-ray-rocking curves shown in Fig 4.6. For samples that contain periodic material variations, as in the MQW samples discussed here, subsequent

diffraction peaks are observed whose positions can be used to determine the thickness and composition.

In Fig 4.6, clear, well-defined diffraction peaks are observed which indicate a high structural quality for the MQW samples. Strain relaxation or severe nitrogen diffusion from layer to layer is not present, as this would result in a much reduced peak contrast. Table 4.4 below gives the composition and width data extracted using fits to the x-ray data.

Sample No.	GaAs Width (nm)	GaAsN Width (nm)	% Nitrogen
00-056	7.44	6.02	0.75%
00-057	6.91	5.63	1.6%
00-058	7.57	5.73	2.6%
00-059	6.99	5.61	4%
00-060	6.64	5.62	3.3%
00-061	6.83	5.43	4.1%
00-062	7.03	6.19	1.8%

Table 4.4: Nitrogen composition and well width extracted from x-ray data for GaAsN MQWs.

Optical Studies

Low temperature photoluminescence data from the MOCVD GaAsN MQW samples is shown below in Fig 4.7. Note that the measurements are presented on a logarithmic scale. Apart from the GaAs band edge luminescence around 1500meV and the broad defect peak around 1470meV, which can be associated with the GaAs material, we observe luminescence only from sample 00-056, with a nominal nitrogen concentration of 1%. For sample 00-056, we assume that the broad peak around 1300meV arises from emission in a region of dilute nitrogen. For samples with greater than 1% nitrogen we

observe no luminescence that can be associated with nitrogen containing material. This lack of luminescence is found to persist even when pumping with greater than 200mW of laser power into a 100micron spot!

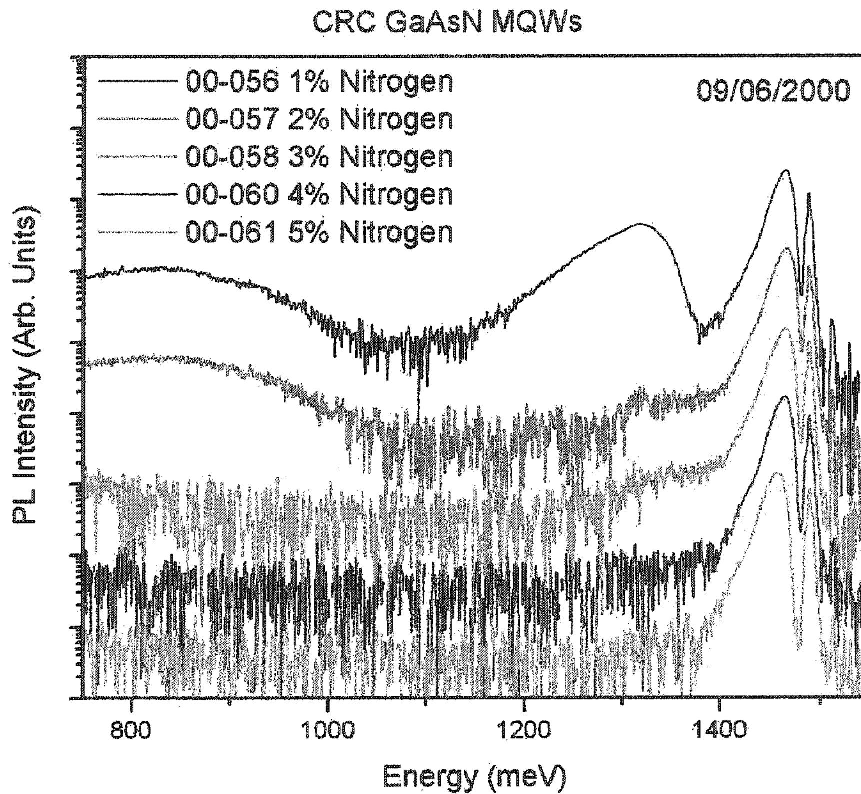

Fig. 4.7 Low temperature photoluminescence from as grown MQW GaAsN samples. Luminescence was excited using 5mW of Ar^+ pump power with a 100μm spot size at 4.5K. FTIR detection using an InGaAs detector was accomplished at a resolution of $8cm^{-1}$ and 20 averaged scans.

The lack of GaAsN related luminescence from these MQW samples is surprising considering the intense luminescence that was observed from single well samples in the same range of composition and considering that the x-ray measurements have confirmed the high structural quality of the samples. To improve the optical properties, annealing experiments were attempted using the rapid thermal annealing capability described in

chapter 3. Fig 4.8 below shows luminescence collected from the MQW samples after annealing at 625°C for 10 seconds.

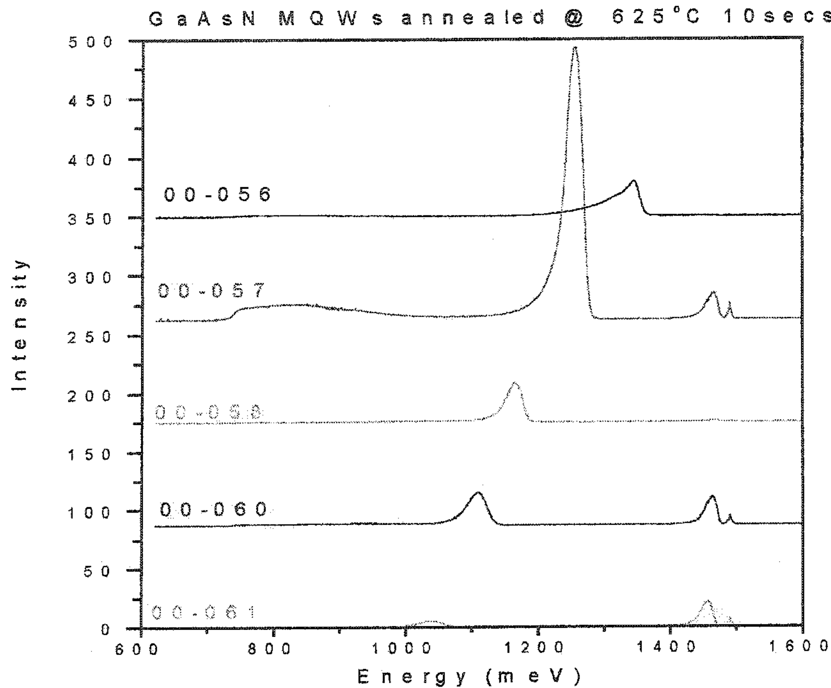

Fig. 4.8: Low temperature photoluminescence from GaAsN MQW samples annealed at 625°C for 10 seconds. Experimental conditions were the same as those described above in fig 4.7.

Following annealing, strong luminescence from the GaAsN material is easily observed. Strong improvements can be seen in all samples, whilst the change in emission energy as a function of nitrogen concentration can be clearly seen to follow the trend expected from Table 4.4. The sample showing the greatest improvement in luminescence efficiency is sample 00-057 (%N=1.6), although it is unclear why this sample is considerably brighter than others.

Annealing Experiments

To further investigate the effects of annealing, a set of experiments were performed in which the time and temperature of the anneals were separately varied. For the set of temperature experiments, temperatures between 500°C and 700°C were chosen, with a fixed time of 10 seconds. This temperature range was chosen to lie between the sample growth temperature and the temperature where quantum well intermixing might be expected to begin [9]. For experiments that involved time variation, the chosen range was between 10 seconds and 360 seconds, with a fixed temperature of 600°C.

(i) Experiments vs Anneal Time

Figure 4.9 shows a representative luminescence spectrum from sample 00-056 after annealing at 600°C for 30 seconds. The luminescence is considerably stronger than

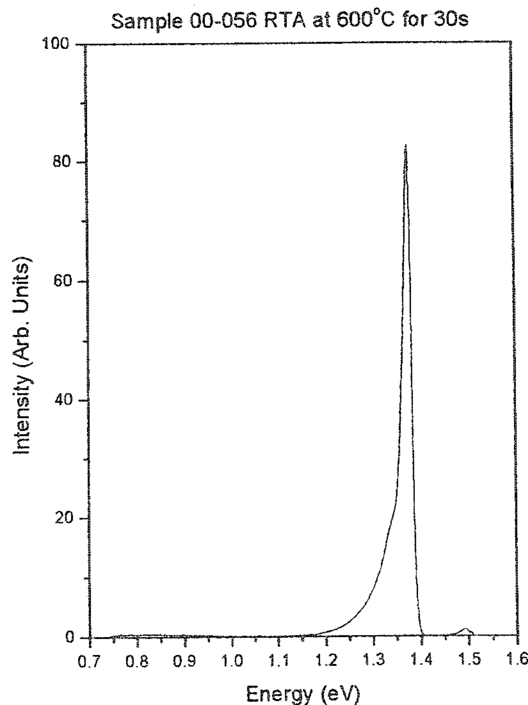

Fig. 4.9: Low temperature photoluminescence data from sample 00-056 after annealing at 600°C for 30 seconds

observed in the unannealed sample, but the improvement in photoluminescence efficiency is a strong function of the anneal time, as shown below in fig 4.10.

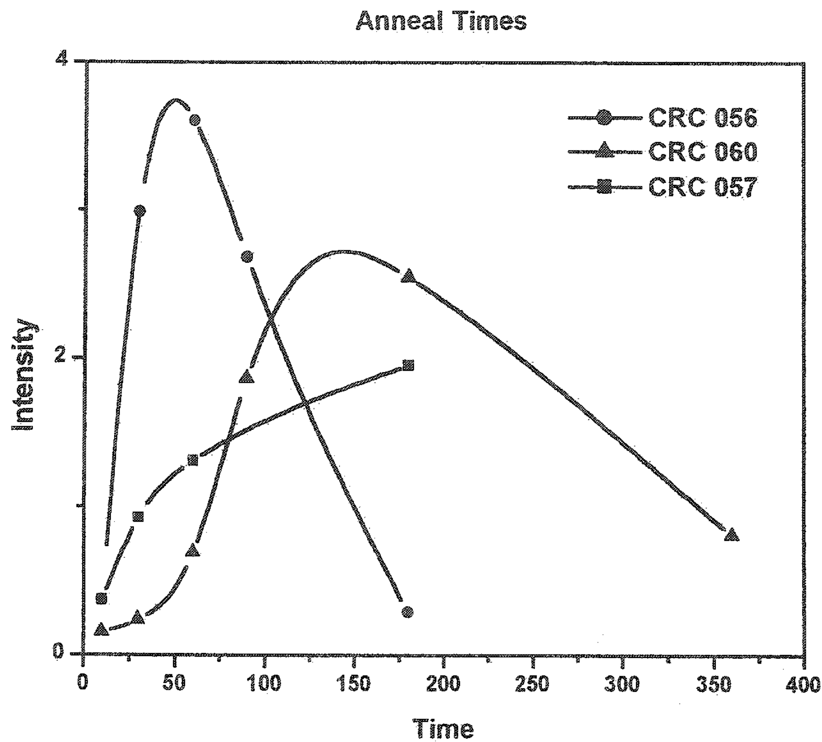

Fig. 4.10: Variation of integrated photoluminescence intensity with anneal time for MQW GaAsN samples annealed at 600°C.

A basic trend can be seen for these samples in that as the anneal time increases, the photoluminescence intensity increases before eventually falling again. For sample 00-057, the photoluminescence intensity continues to rise monotonically over the time range investigated.

(ii) Experiments vs Anneal Temperature

Figure 4.11 shows representative photoluminescence data from sample 00-057 after a 10 second anneal at different temperatures.

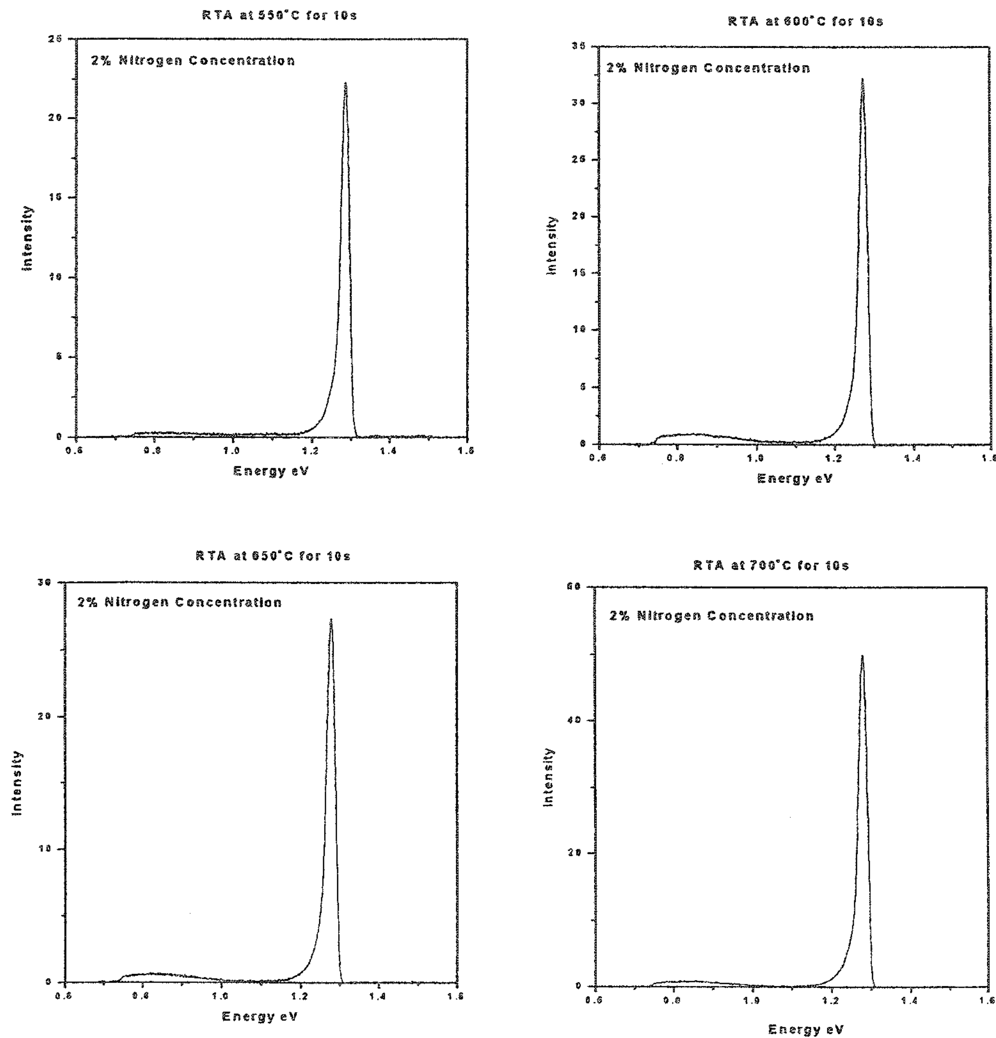

Fig. 4.11: Low temperature photoluminescence from sample 00-057 after a series of 10 second anneals at different temperatures.

At the lowest anneal temperature (500°C – data not shown), the GaAsN luminescence is again very weak and indeed it is comparable to the band edge GaAs luminescence. For all higher anneal temperatures, the GaAsN luminescence is seen clearly around 1.28eV and does not shift substantially as a function of temperature.

Figure 4.12 shows the variation of integrated intensity with anneal temperature for the different MQW samples. All measurements were taken at 4K with 2mW of Ar^+ laser excitation. Apart from the anomalous behaviour of sample 00-056, which has an intensity that peaks at 600°C anneal temperature, the samples show a monotonic rise in integrated PL intensity with increasing anneal temperature. The last temperature for this series is 700°C. It is likely that further increases in anneal temperature will produce further improvements in the PL efficiency, but this may come at the expense of a blue-shifted luminescence arising from quantum well intermixing effects as mentioned previously.

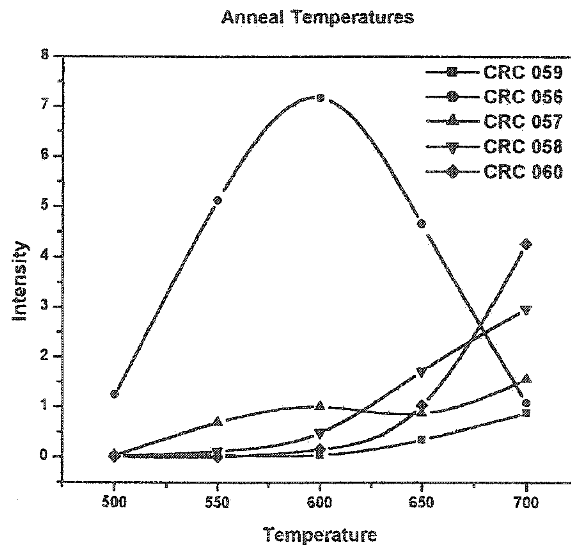

Fig 4.12: Variation of integrated intensity with anneal temperature for GaAsN multiple quantum wells.

4.1.3 Absorption Measurements of GaAsN grown by MOVCD

With the availability of GaAsN multiple quantum well samples, absorption experiments were performed to compare the band edges measured using absorption and PL. As discussed previously, PL measurements are expected to emphasize the lowest lying states, so that differences between PL and absorption might be expected if samples show local variations in the bandgap, from alloy variations for example. Such differences, between absorption and PL, are commonly referred to as a Stokes shift. In many, highly uniform, III-V semiconductors, the Stokes shift can completely vanish or may be very small, on the order of a few meV, in the presence of localised defect states [10].

In Fig 4.13 we show low temperature absorption measurements from some of the GaAsN MQW samples, along with the corresponding PL measurements. The red line in the graphs shows absorption, whilst the black line shows the PL. In all cases, the absorption measurement shows an edge to higher energy than the corresponding PL measurement, suggesting that a high degree of band edge non-uniformity exists in these samples. Indeed, in some cases the Stokes shift exceeds 100meV, which is extremely large for normal III-V materials. In addition, the Stokes shift seems to increase as the nitrogen concentration increases. In addition to the possibility of a large degree of alloy non-uniformity, which might not be surprising in material grown at such a low temperature, it is possible that the large Stokes shift appears as the result of a native defect below the bulk band edge. Such states have been suggested as arising in Indium

containing material [11-14] due to local variations in the N-In and N-Ga bonding ratio, although this mechanism would not seem to be valid in GaAsN.

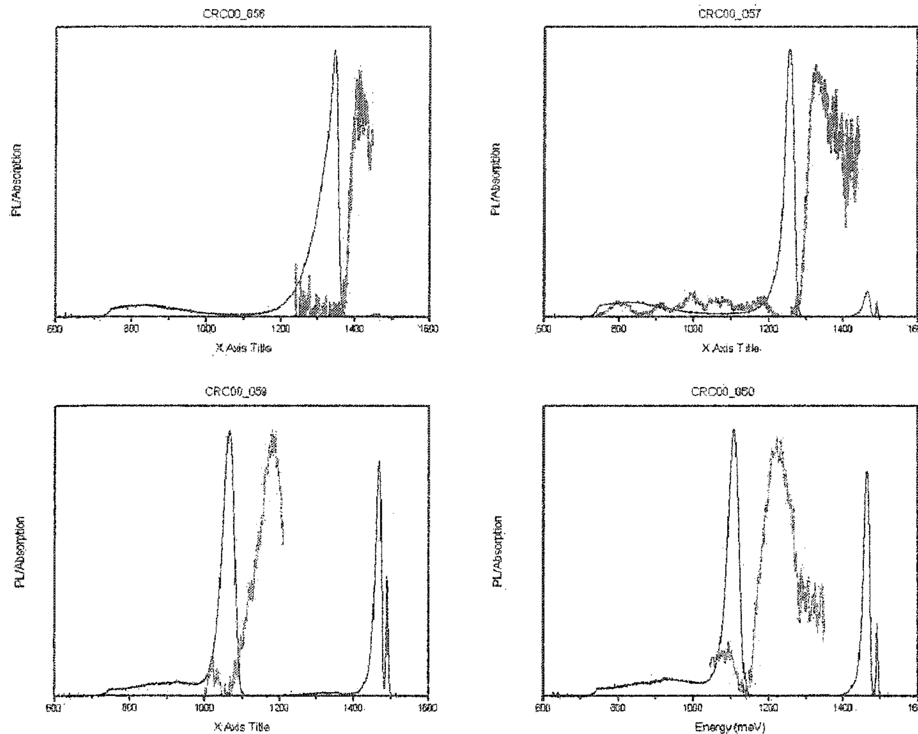

Fig 4.13: Comparison of absorption and PL measurements. Data is obtained at 4K with a broadband light source.

4.1.4 PLE measurements of MOCVD grown GaAsN

For comparison with the absorption measurements, PLE measurements were conducted on the MQW MOCVD samples. These types of measurements proved to be extremely difficult because the laser that was chosen could not scan the whole wavelength range for the samples that were grown. One sample, 00-057 with 2% nitrogen, did lie within the specific tuning range that was available. Figure 4.14 below

shows PLE data collected from this sample for a detection energy of 1240meV and a minimum excitation energy of 1254meV.

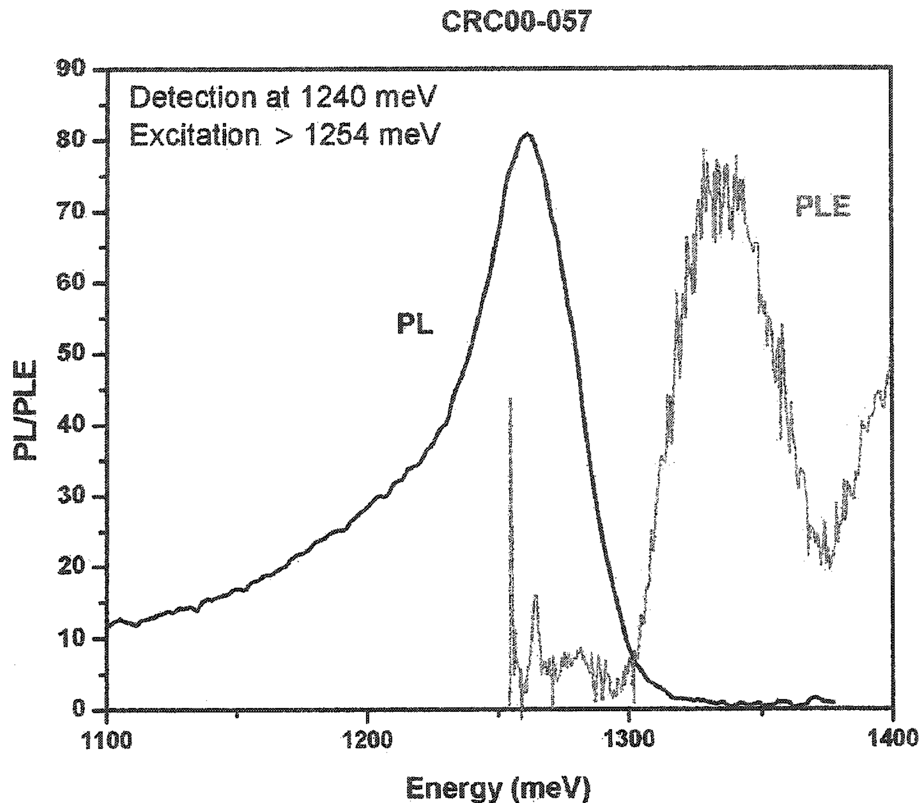

Fig. 4.14: Comparison of PL and PLE measurements for sample 00-057. Measurements were performed at 77K with a laser power of 60mW

The PLE measurements again show a band edge shifted to substantially higher energy than the PL measurements, so that we can have some confidence that the data measured in absorption is valid. It is also important to realise that the PLE measurements indicate that there must be some mechanism for carrier transfer between the 'place' where carriers were generated, i.e. at high energy, and the 'place' where recombination is detected, i.e. at lower energy. If the large Stokes shift that is observed in these samples is

a result of composition inhomogeneity, then carriers must be able to diffuse readily to places of lower bandgap.

In addition to the main PLE peak at approximately 1340meV, a relatively sharp peak is observed to lower energy, at approximately 1265meV. This peak is interesting and deserves further investigation if the quality of the PLE measurements can be improved. Such a peak may represent an excited state of some type of quantum dot structure, produced as a result of the large compositional fluctuations. However, further measurements are required to ensure that this peak is not a result of stray light from the laser source.

4.2 MBE GaAsN

4.2.1 Single Wells

GaAsN material has been grown by Dr. J. Gupta and Dr. Z. Wasilewski at the National Research Council (NRC), Institute for Microstructural Sciences using the modified VG V80H molecular beam epitaxy (MBE) system described in chapter 1. The growth of these samples represents the first time that dilute nitride materials were grown at the NRC.

Figure 4.15 below shows low temperature photoluminescence from a GaAs sample grown in the MBE system when the nitrogen plasma source was operating, but with the shutter to the cell closed. In addition to the expected GaAs features around 1.5eV, a broad emission peak is observed centered at 1.4eV on top of which we observe a series of sharp emission lines. This data leads one to believe that the mechanical shutter in front of the nitrogen source is not completely effective at isolating the supply of

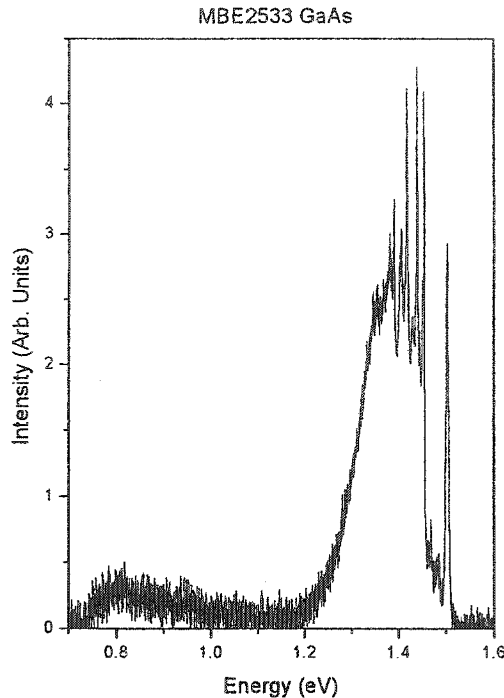

Fig. 4.15: MBE GaAs sample grown with the Nitrogen plasma source operating but the shutter closed.

nitrogen. Instead, a continuous low concentration of nitrogen is supplied to the growing GaAs layer that results in the observed emission. Sharp emission features such as those in Figure 4.15 have been observed previously in GaAs samples doped with extremely low concentrations of nitrogen [15 - 18], where they have been associated with nitrogen clusters with varying numbers of nitrogen atoms and configurations.

A sequence of single quantum well GaAsN samples was grown by MBE to determine the appropriate conditions under which to grow the material. The growth parameters for these samples are given in table 4.5 below,

Sample No.	GaAs (nm)	GaAsN (nm)	Temp (°C)	RF Power (W)	% Nitrogen
2526	90	35	470	200	0.34%
2527	90	35	470	350	0.55%
2528	90	35	470	500	0.60%
2529	99.3	33.1	470	200	1.58%
2531	99	32.6	470	350	1.115%
2532	96.2	34.4	470	500	0.88%

Table 4.5: Sample parameters for MBE GaAsN Quantum Well Samples

Each sample consisted of a single GaAsN quantum well of thickness approximately 35nm, separated from the surface by approximately 90nm of GaAs. The samples were grown at 470°C using a sequence of different RF powers. Low temperature photoluminescence from these samples is shown below in Fig 4.16. The data was taken at 4K using 2mW of Ar^+ excitation. In addition to the GaAs related features, we see luminescence below the GaAs bandgap that we associate with the GaAsN quantum well. In each sample there is a clear single peak at higher energy and a very broad feature centered around approximately 0.85eV. We assume that the higher energy peak is related to the main GaAsN quantum well bandgap and indeed, the energy of this feature seems to follow the trend of nitrogen concentrations given in table 4.5 above. However, this bandgap-related photoluminescence is very weak and is of comparable intensity to the lower energy emission and to the bulk GaAs related features around 1.5eV. No clear trend with RF power is observed.

In Fig 4.17 we add the data obtained from these MBE samples for the GaAsN bandgap as a function of nitrogen concentration to the previous data obtained for MOCVD samples.

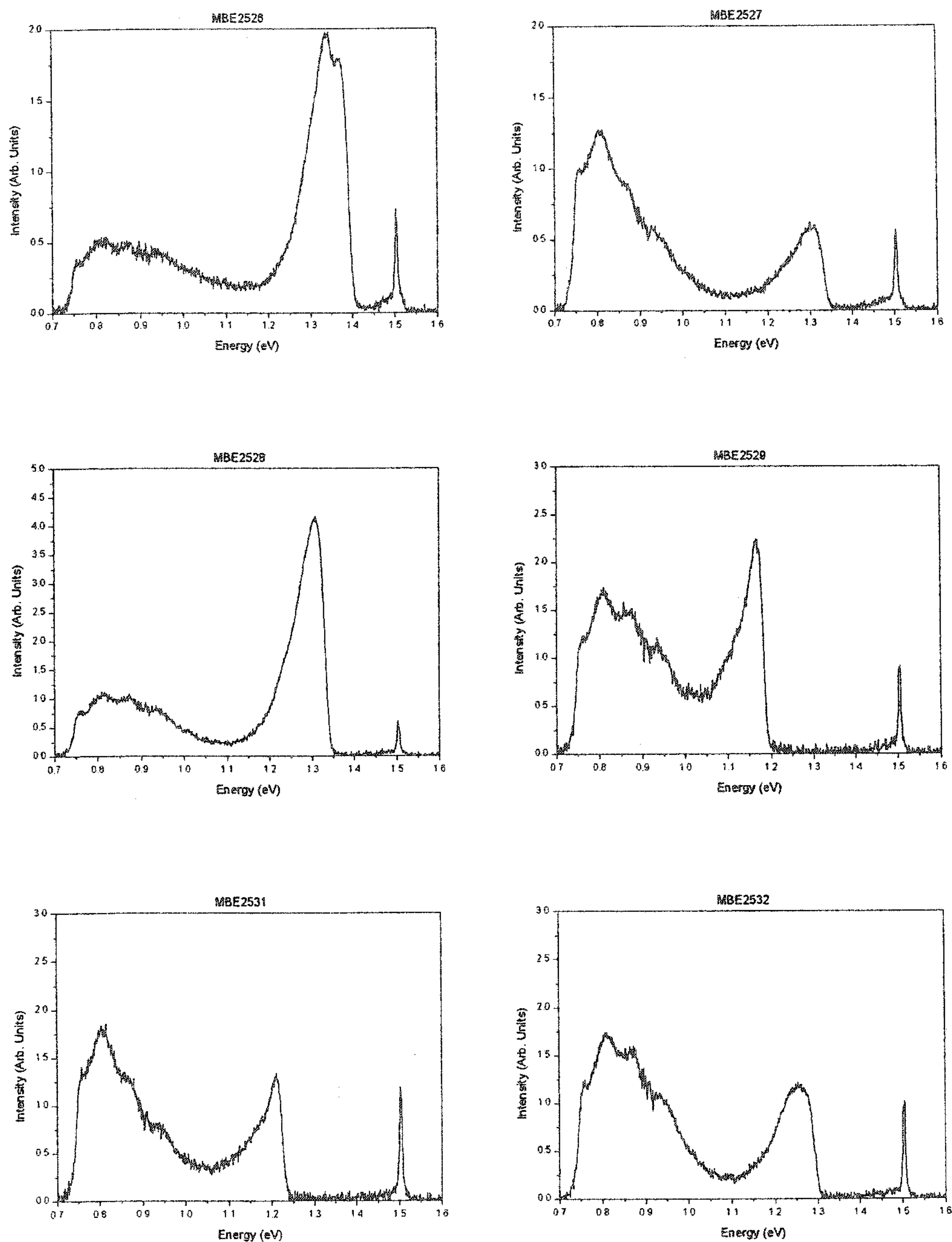

Fig 4.16: Low temperature photoluminescence from MBE GaAsN samples grown with varying RF power.

Although the bandgap obtained from the MBE samples shows a steady reduction with increasing nitrogen concentration, with a gradient that is approximately equal to that obtained for the MOCVD samples, it is clear that there is an offset along the composition

axis. Such a shift could result from the steady leak of nitrogen around the shutter that was discussed above.

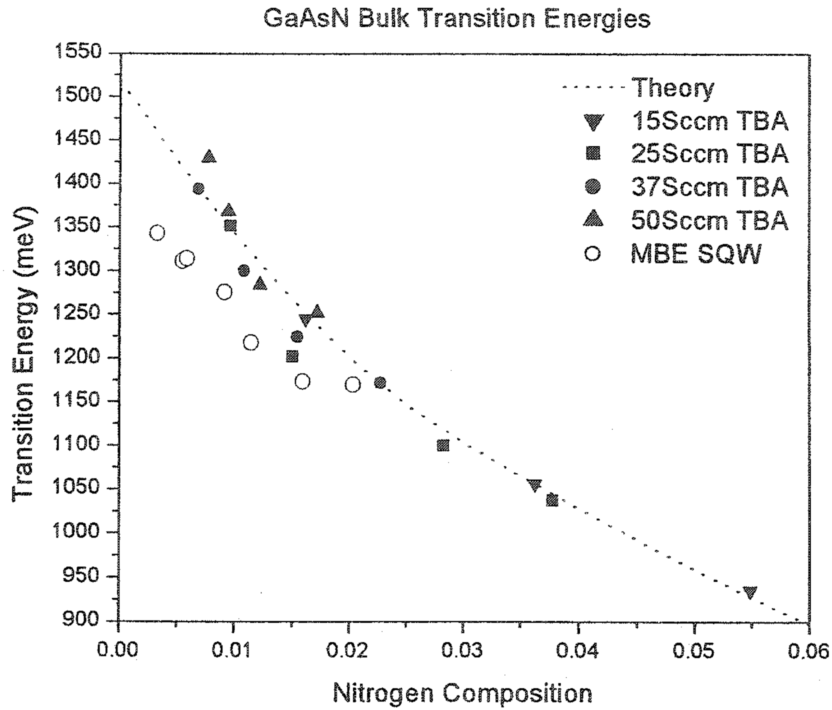

Fig. 4.17: Comparison of GaAsN bulk bandgap obtained from MOCVD and MBE material.

In an attempt to improve the luminescence intensity, a series of annealing experiments were done in the temperature range between 650°C and 850°C. Representative data from sample MBE2529 is shown below in Fig 4.18. The data is plotted so that the changes produced by annealing are easily observed. The photoluminescence measurements were again taken at 4K using 2mW of Ar^+ excitation. For annealing temperatures up to 750°C, the luminescence intensity increases monotonically, as seen previously for MOCVD material, although the effects of annealing do not seem to be as strong for the MBE material.

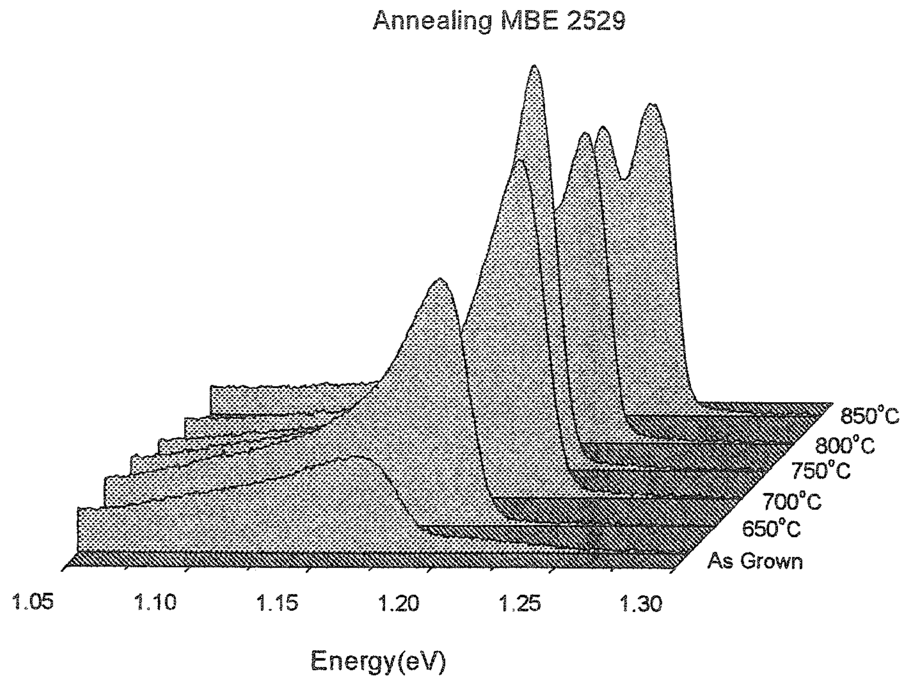

Fig. 4.18: Photoluminescence measurements on MBE 2529 after rapid thermal annealing at a variety of temperatures for 60 seconds.

Above 750°C, the peak intensity diminishes and the luminescence develops an unusual two-peaked structure. The photoluminescence from the 850°C annealed sample is shown in Fig 4.19 as a function of pump intensity. As a function of increasing pump intensity, the higher energy peak of the two begins to dominate the spectrum. The origin of this unusual behaviour is not clear, but we might speculate that on annealing at high temperatures, the sample begins to develop small regions of nitrogen clusters, which produce reasonably strong low temperature photoluminescence as carriers migrate around to find the lowest energy regions. However, if these clusters are produced only in low concentration, then we would expect the luminescence from higher energy transitions to

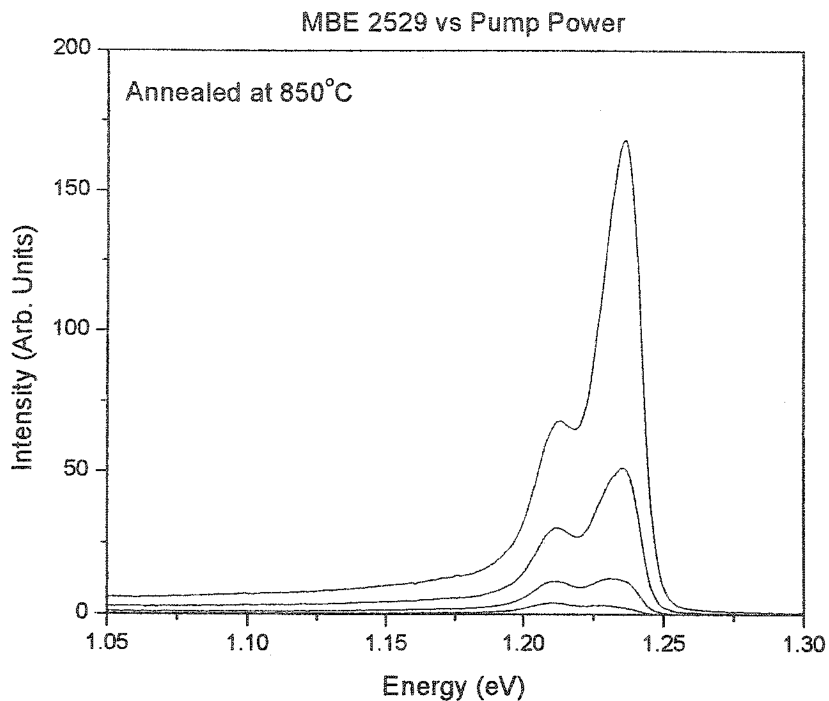

Fig. 4.19: Low temperature photoluminescence from sample MBE 2529 after annealing at 850°C for 60 seconds. The four sets of data correspond to pump powers of 0.61mW, 2mW, 6mW and 18mW.

increase in importance as the pump power is increased and the cluster luminescence begins to saturate.

4.2.2 PLE measurements of MBE grown GaAsN

Photoluminescence excitation measurements were attempted using MBE 2529 to determine whether the large Stokes shift that was observed for MOCVD samples was reproduced in the MBE samples. Figure 4.20 below shows PLE data collected from a sample annealed at 850°C for 60 seconds, with a detection energy of 1233meV and a minimum excitation energy of 1240meV.

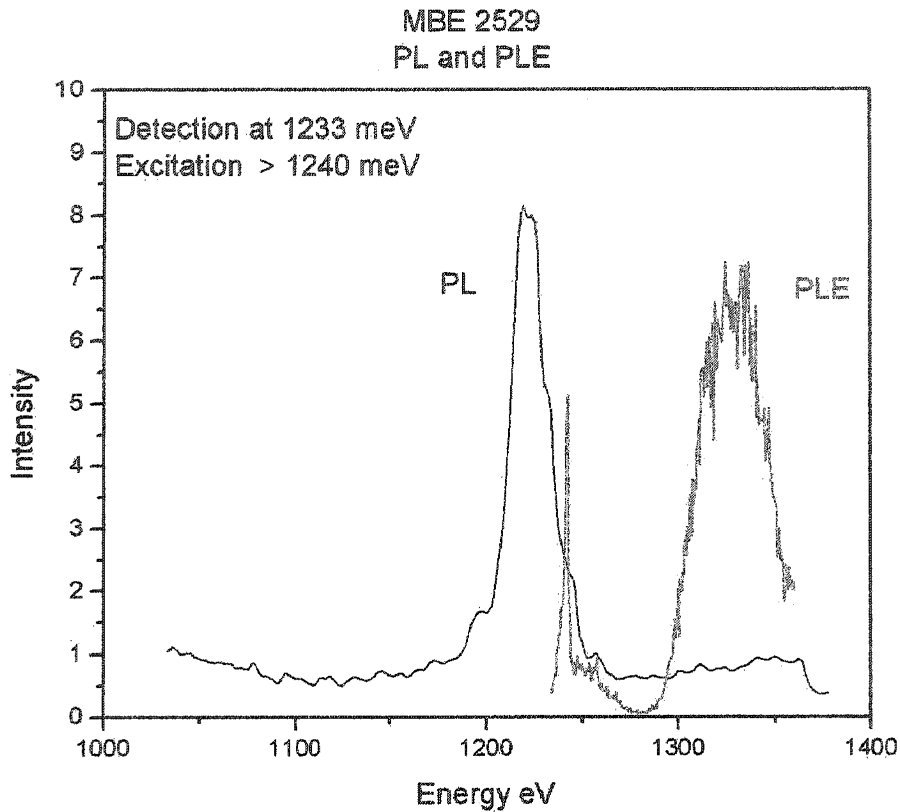

Fig. 4.20: Comparison of PL and PLE measurements for sample MBE 2529 after annealing at 850°C for 60 seconds. Measurements were performed at 77K with a laser power of 44mW.

At this measurement temperature, the annealed sample does not show the double-peaked emission spectrum discussed above. This may occur because of the easy thermal activation out of the lower energy state at this temperature. However, the large Stokes shift observed previously for the MOCVD material is seen also in the MBE material, indicating that this effect is universal and not specific to the particular type of GaAsN growth used. A very sharp emission line below the main bandgap is again observed in the PLE data.

4.3 Conclusions

In this chapter we have determined the band edge emission characteristics of single and multiple quantum well GaAsN material grown by both MBE and MOCVD. Photoluminescence, photoluminescence excitation and absorption measurements have been performed and indicate the presence of a large Stokes shift.

Rapid thermal annealing has been used to improve the luminescence efficiency, and to reduce the full width at half maximum, although the improvements seem to be substantially larger in the MOCVD material. Substantial blue shifts of the emission energy are observed for anneal temperatures in excess of approximately 750°C.

References

[1] B. Hamilton, in *Properties of Gallium Arsenide*: 3rd edition, M.R. Brozel and G.E. Stillman (Eds.) (INSPEC, England, 1996).

[2] J.A. Gupta, W.R. McKinnon, J. Noad, D. Coulas, R.L. Williams, R. Driad, S.P. McAlister, Journal of Crystal Growth, **231**, 48 (2001).

[3] H. Dumont, L. Auvray, Y. Monteil, and J. Bouix, Materials, Science, and Engineering B, **84**, 258 (2001).

[4] L. Auvray, H. Dumont, J. Dazord, Y. Monteil, J. Bouix, C. Bru-Chevallier, L. Grenouillet, Materials science in semiconductor processing, **3**, 505 (2000).

[5] B. Gil, Solid State Communications, **114**, 623 (2000).

[6] G. Pozina, I. Ivanov, B. Monemar, J. Thordson, and T. G. Andersson, Materials, Science, and Engineering B, **50**, 153 (1997).

[7] Y. Zhang, A. Mascarenhas, H. P. Xin and C. W. Tu, Phys. Rev. B 63, 161303(R) (2001).

[8] BEDE Scientific, Inc. UK.

[9] S. Charbonneau, P. J. Poole, P. G. Piva, G. C. Aers, E. S. Koteles, M. Fallahi, J.J. He, J.P. McCaffrey, M. Buchanan, M. Dion, R. D. Goldberg and I. V. Mitchell, J. Appl. Phys. **78** (6), (1995).

[10] J. I. Pankove *Optical Processes in Semiconductors*, (Dover Publication, New York, 1971).

[11] S. Kurtz, J. Webb, L. Gedvilas, D. Friedman, J. Geisz, J. Olson, R. King, D. Joslin, and N. Karam, Appl. Phys. Lett. **78**, 748 (2001).

[12] P. J. Klar, H. Gruning, J. Koch, S. Schafer, K. Volz, W. Stolz, W. Heimrodt, A. M. Kamal Saadi, A. Lindsay, and E. P. O Reilly, Phys. Rev. B 64, 121203(R) (2001).

[13] S. A. Choulis, T. J. C. Hosea, P. J. Klar, M. Hofmann, and W. Stolz, Appl. Phys. Lett. 79, 4277 (2001).

[14] S. Kurtz, J. F. Klem, A. A. Allerman, R. M. Sieg, C. H. Seager, and E. D. Jones, Appl. Phys. Lett. 80, 1379 (2002).

[15] D. J. Wolford, J. A. Bradley, K. Fry, J. Thompson, and H. E. King, in *Gallium Arsenide and Related Compounds*, edited by G. E. Stillman, Inst. Phys. Conf. Ser. No. 65 (The Institute of Physics, Bristol, 1983), p. 477; in *Proceedings of the 17th International Conference on the Physics of Semiconductors*, edited by J. D. Chadi and W. A. Harrison (Springer, New York, 1984), p. 627.

[16] M. Leroux, G. Neu, and C. Vèrié, Solid State Commun. **58**, 289 (1986).

[17] X. Liu, M.E. Pistol, L. Samuelson, S. Schwetlick, and W. Seifert, Appl. Phys. Lett. **56**, 1451 (1990); X. Liu, M.E. Pistol, and L. Samuelson, Phys. Rev. B **42**, 7504 (1990).

[18] Yong Zhang, A. Mascarenhas, J. F. Geisz, H. P. Xin and C. W. Tu, Phys. Rev. B 63, 085205 (2001).

Chapter 5

InGaNAs

This chapter describes the optical characterisation of InGaAsN material grown by both MOCVD and MBE. In the case of MBE material we discuss the photoluminescence characterisation of the initial material grown at NRC and use growth without sample rotation to achieve a large variation in material composition. Experiments are also performed as a function of sample temperature and a model is proposed to explain the observed low temperature photoluminescence quenching behaviour.

5.1 MOCVD InGaAsN

A set of four, single quantum well, InGaAsN samples were grown by MOCVD with the characteristics described in table 5.1 below. Each sample was composed of a nominally 20nm quantum well, separated from the surface by a 100nm GaAs cap layer and was grown with a TMG flow of 5Sccm, a TBA flow of 15Sccm, a TMI flow of 50Sccm and a DMHy flow of 100Sccm.

Sample No.	Growth Temp. (°C)	%N	%In
01-041	510	1.13	25.7
01-042	520	1.7	26.9
01-043	530	1.7	28.3
01-044	550	0.59	29.7

Table 5.1: Sample design for single quantum well InGaAsN samples

The growth conditions chosen for these samples are similar to those for the GaAsN series 00-031 to 00-034 discussed previously, with the added flow of TMI required for the inclusion of Indium. Sample 00-031, which was also grown with a DMHy flow of 100Sccm was found previously to display no photoluminescence, because of relaxation due to the high level of strain. The inclusion of Indium is expected to reduce this strain and consequently improve the optical quality.

Representative photoluminescence spectra from these samples are shown in Fig. 5.1 below. Measurements were conducted at 4K with 2mW of HeNe excitation. 20 scans were averaged with a resolution of $8cm^{-1}$. Prior to annealing, the luminescence from these samples was poor with a broad, low intensity signal that covered the region between 0.7eV and 1.3eV in addition to the GaAs related features around 1.5eV. Annealing at

600°C for 30 seconds was found to improve the luminescence considerably, although a relatively broad signal was still seen in all samples.

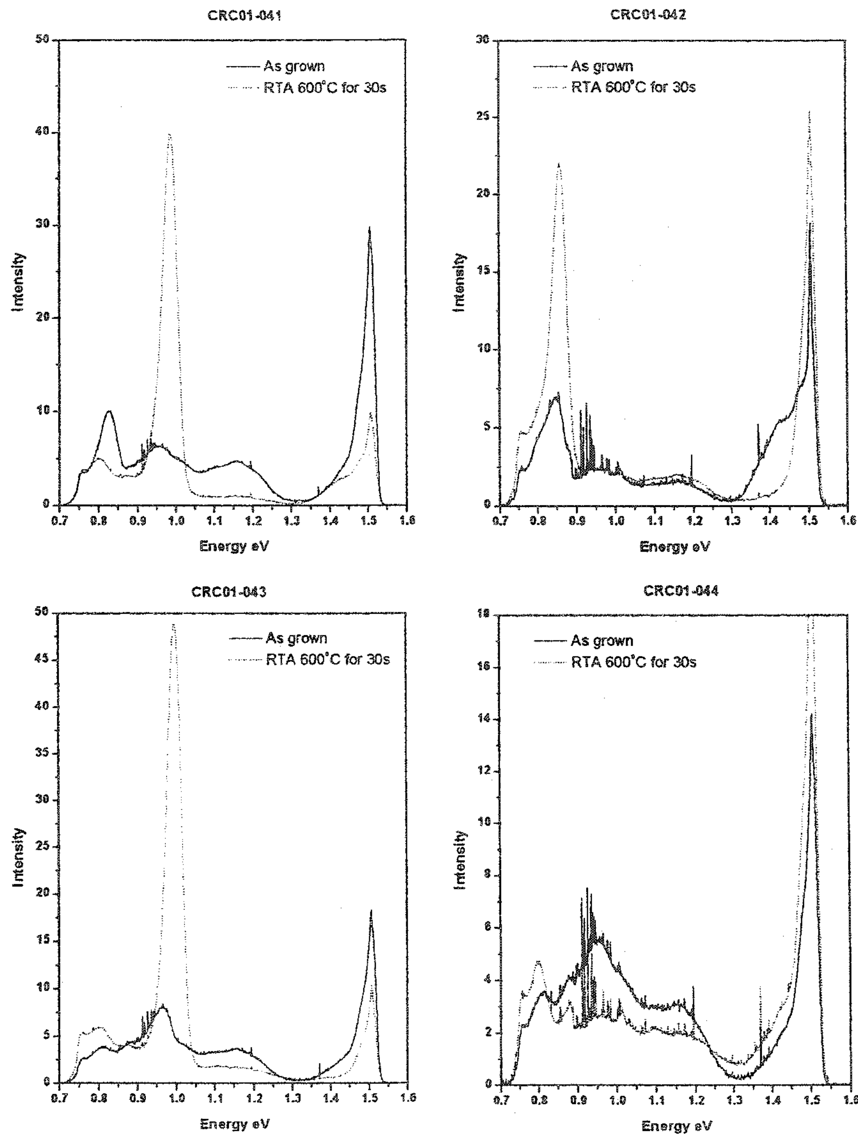

Fig. 5.1 Photoluminescence (PL) from single quantum well InGaNAs samples. PL from annealed samples is shown dotted.

After annealing, three of the four samples show a single peak that is much stronger than any adjacent emission, which we associate with the InGaAsN. Sample 01-

044, with the highest growth temperature and highest Indium concentration, still shows broad luminescence, without a dominant InGaAsN emission peak. Even after annealing, the optical quality of these samples was still not high and the behaviour was hard to understand in any detailed way. In consequence, it was decided to grow a further set of samples with a lower Indium concentration.

The second set of InGaNAs samples were again grown with a nominally 20nm wide quantum well and a nominally 100nm thick GaAs cap layer. The Indium composition was fixed at eight percent, whilst the nitrogen concentration was varied. The gas flows used in the growth were 5Sccm, 15Sccm and 15Sccm respectively for the TMG, TBA and TMI. The samples are described in table 5.2 below.

Sample No.	Growth Temp. (°C)	%In	DMHy (Sccm)
01-052	525	8	80
01-053	525	8	70
01-054	525	8	60

Table 5.2: Sample design for second set of InGaAsN samples

As seen in Fig 5.2 below, the photoluminescence from the two lower nitrogen concentration samples, taken under the same conditions that were described above, was much improved. Both of these lower nitrogen concentration samples show a dominant InGaNAs related peak before annealing whose intensity is increased upon annealing at 600°C for 30 seconds. For sample 01-052 a peak around 1eV becomes prominent only after annealing, whilst strong intensity luminescence to lower energy is still observed. Indeed, in all of the MOCVD InGaAsN samples, strong luminescence is observed below what we might conclude is the dominant band gap.

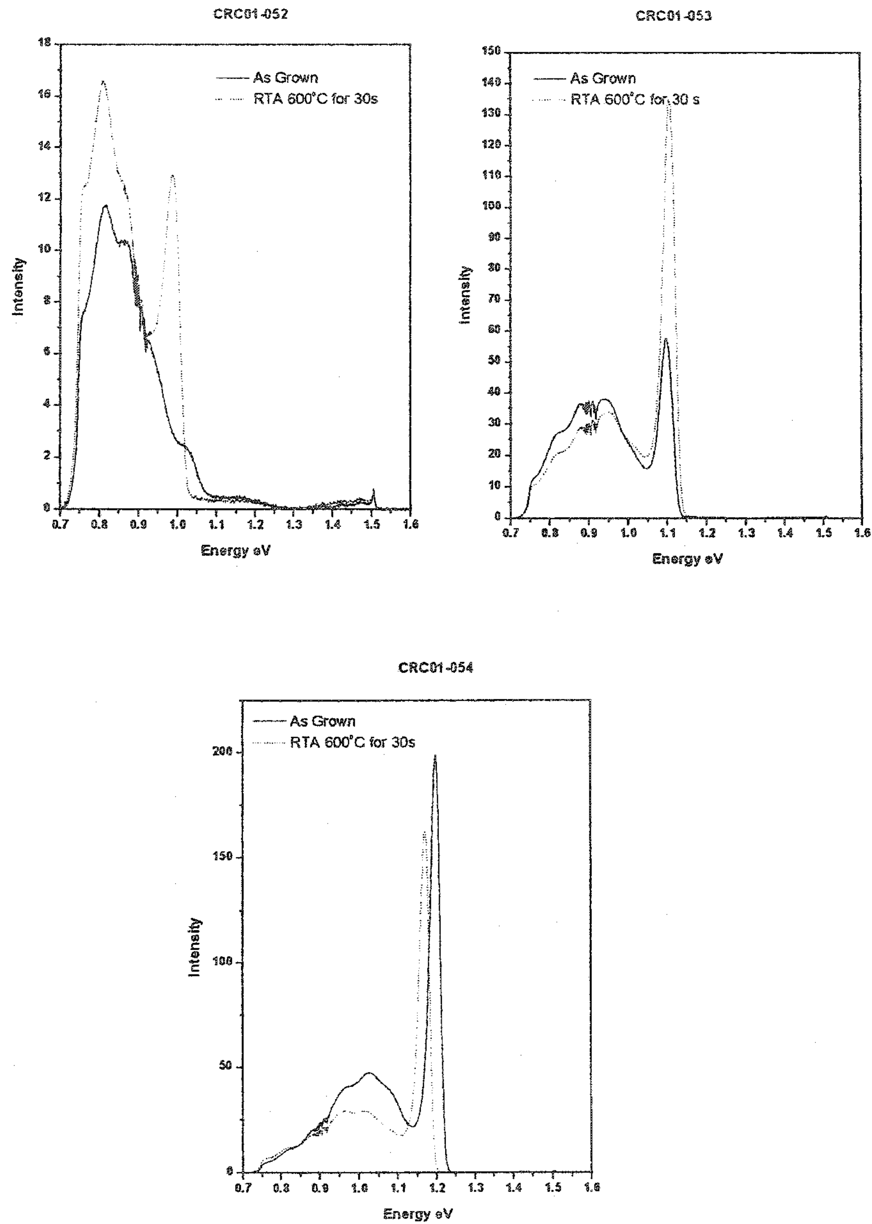

Fig. 5.2: Photoluminescence from nominally 8% In containing InGaAsN samples.

As mentioned above, such effects have been extensively observed in InGaAsN material and have been attributed to variations in the local bonding configuration of N, between N-In and N-Ga [1-5].

5.2 MBE InGaNAs

5.2.1 Wafer Mapping

In this section we present data on some of the first InGaAsN samples grown by MBE at the NRC. When beginning a study of the growth of this material it is important to establish, as quickly as possible, the conditions under which high optical and structural quality material can be grown. To this end, it was decided to grow a sample in which considerable variations in composition and thickness could be expected across a single wafer. A schematic illustration of the sample is given in Fig 5.3 below.

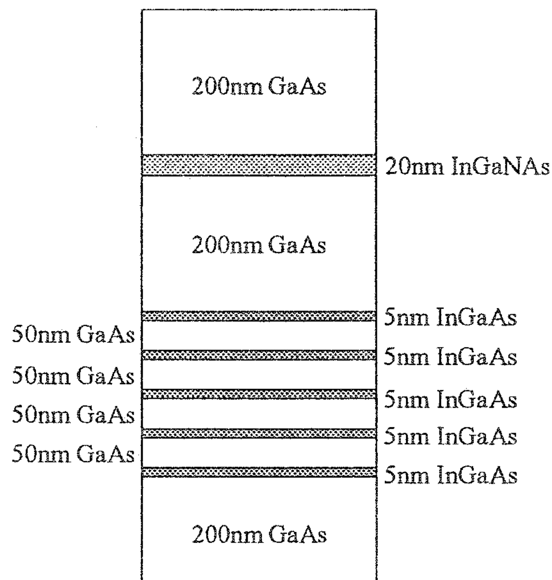

Fig. 5.3: Schematic of the InGaAsN sample grown on a non-rotating substrate.

To achieve the large variations in composition and thickness that were required, the sample was not rotated in the conventional way during growth, so that large variations in the elemental fluxes were produced across the wafer. To calculate the In flux incorporated into the structure, a five period InGaAs MQW was included in the

design, so that x-ray measurements, performed by Dr. James Gupta at the NRC, could be used to deduce the In concentration. In this way, independent calculation of the Indium and nitrogen concentrations in the InGaAsN layer of interested could be achieved.

X-ray Results

Fig 5.4 below shows the variation of Indium concentration in the InGaAs ternary layers across the wafer, as determined from the x-ray measurements.

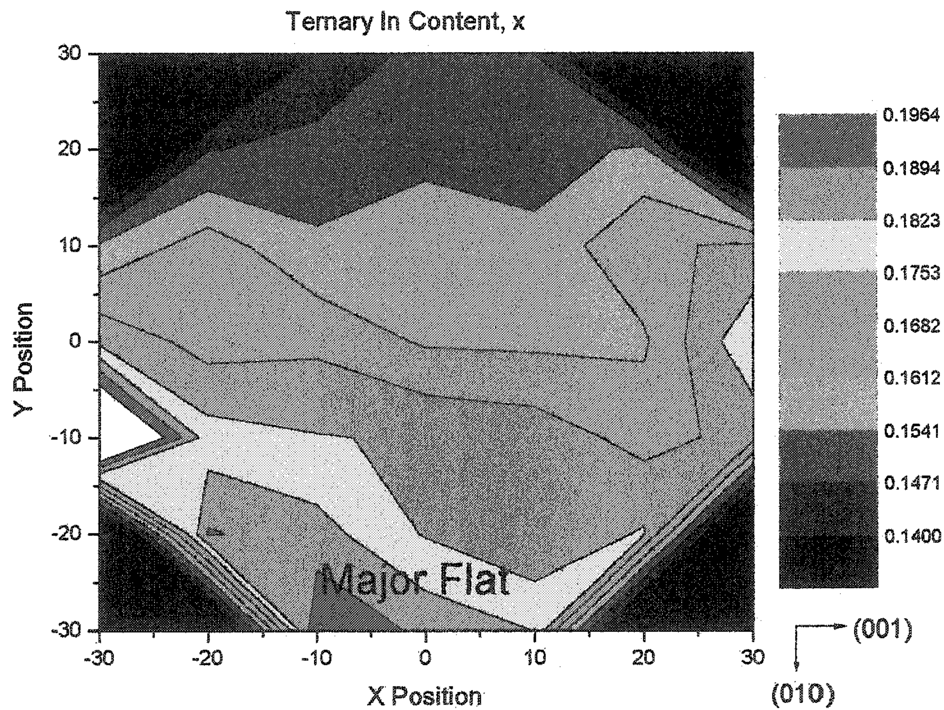

Fig. 5.4: Variation of Indium concentration in InGaAs ternary across the non-rotated substrate, as determined from x-ray measurements. Position in mm.

From the values extracted for Indium composition and similar data for GaAs layer thickness, it is possible to extract the variation in Indium and Gallium flux across the stationary wafer. This calculation is complicated by the presence of Indium segregation in the InGaAs wells, as deposited In rides up on the top surface of the growing layer to produce a position dependent Indium concentration. This effect was taken into account by Dr. Gupta whilst calculating the distribution of fluxes across the wafer, which are needed to calculate the nitrogen fraction in the InGaAsN well.

Figures 5.5 and 5.6 below show the distribution of Indium and nitrogen in the InGaAsN layer as determined from the x-ray data, by taking into account the flux data calculated from the InGaAs wells. Segregation effects were neglected in the InGaAsN well because of its greater thickness. The general shape of the quaternary Indium content distribution closely resembles that for the ternary distribution, with the differences arising

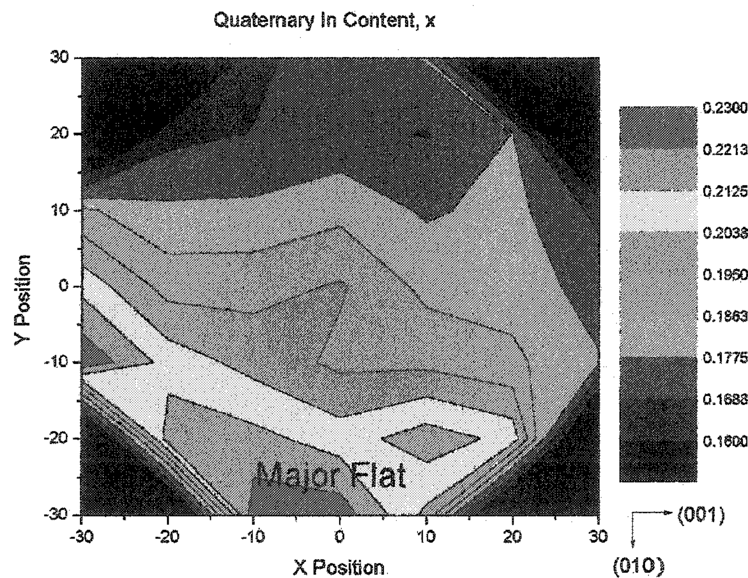

Fig. 5.5: Indium content in the InGaAsN quaternary layer.
Position in mm

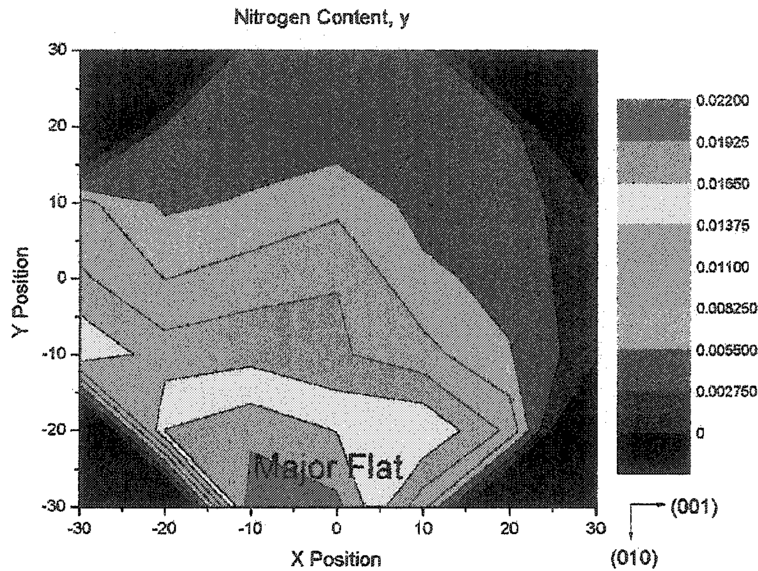

Fig. 5.6: nitrogen content in InGaAsN quaternary layer.
Position in mm.

from the segregation effects. From the top to the bottom of the wafer, along the (010) direction, the Indium concentration varies between approximately 16% and 23%, whilst the nitrogen concentration varies between approximately 0% and 2% over the same distance. Smaller variations are seen along the (001) direction.

Finally, for future use, a model of the MBE growth environment was established by Dr. G.C. Aers at the NRC to allow for future modeling of the alloy composition in InGaAsN material. An example of the output of the calculation for the relative nitrogen content in an InGaAsN layer is shown in Fig 5.7 below. The calculation is found to reproduce the basic trends of the experimental x-ray data.

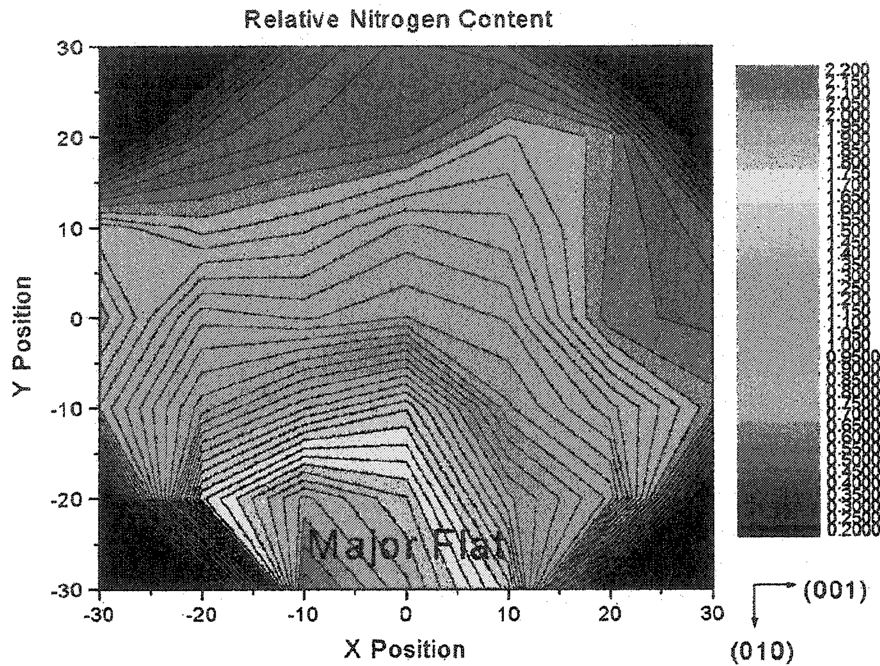

Fig. 5.7: Calculated variation in the nitrogen composition of the InGaAsN sample. Position in mm.

Photoluminescence Measurements

Once the x-ray measurements were completed, the wafer was diced into 5mm x 10mm pieces and low temperature photoluminescence measurements were performed. Measurements were taken at 4K with 2mW of HeNe excitation. Typical data from a single piece of the wafer is shown below in Fig 5.8. The spectrum contains two dominant emission lines that we associate with (A) the InGaAs quantum wells and (B) the InGaAsN layer. Although the integrated intensity for the InGaAs peak is substantially

greater than that for the InGaAsN peak, we must remember that there are five InGaAs wells and only one InGaAsN layer.

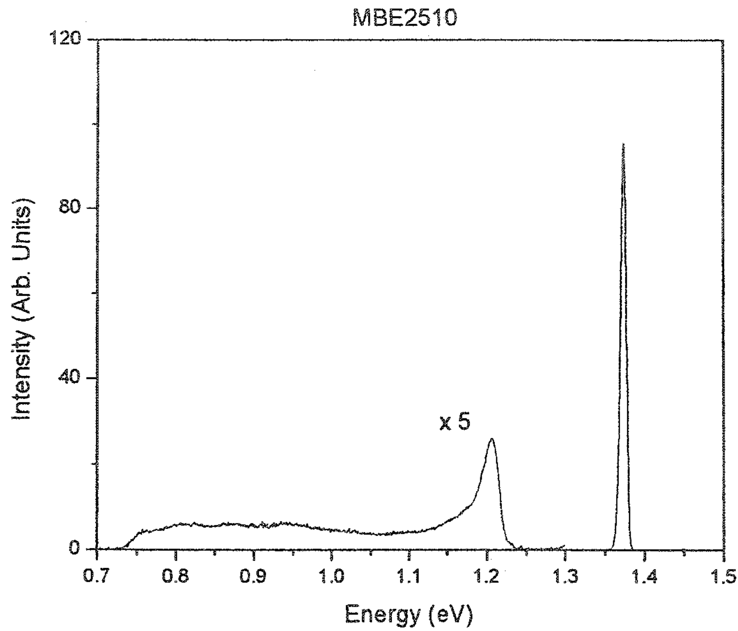

Fig. 5.8: Low temperature PL from a piece of the InGaAsN sample MBE 2510 grown without sample rotation.

(i) Integrated Intensities

Figure 5.9 shows the variation of the integrated intensity of the InGaAs peak with position across the wafer. Apart from one area towards the lower left corner of the wafer, where the intensity is reduced, the integrated intensity varies very little, remaining within a factor of approximately two of the peak intensity. This is encouraging, since more than anything else, it signifies that the alignment of the optical system used for experiments remains fairly consistent from day to day. Apart from this, nothing further should be concluded from the data, since variations in intensity from day to day are very difficult to account for experimentally.

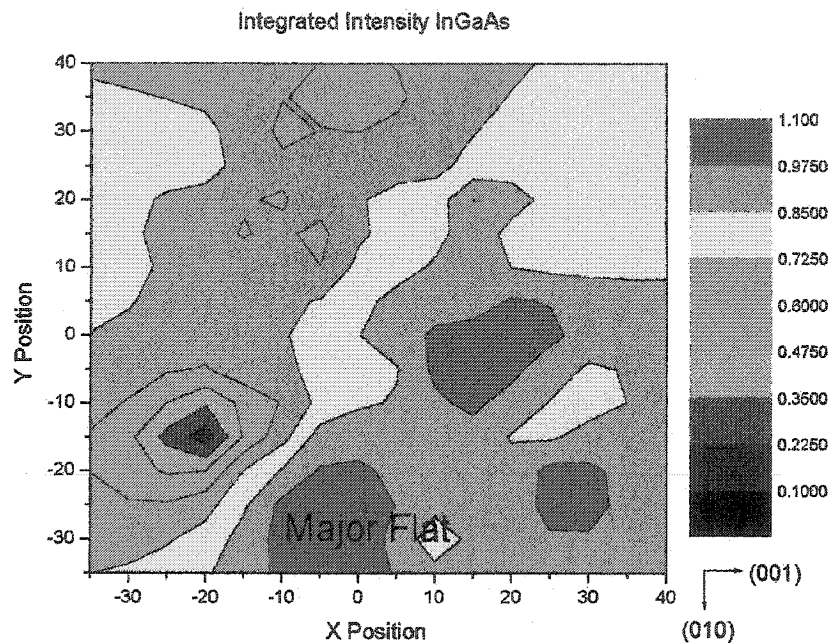

Fig 5.9: Variation of the integrated intensity of the InGaAs peak across the wafer. Position in mm

(ii) Emission Energies

Figure 5.10 shows the variation of the InGaAs peak energy with position across the wafer. The peak energy is lowest in the lower left corner of the figure and increases smoothly along the $(0\bar{1}1)$ direction, with contours of constant energy lying approximately normal to this direction. The shift in energy of the InGaAs peak is a result of changes in both well thickness and Indium concentration. From Fig 5.4 above, we know that the Indium concentration increases from top to bottom along the (010) direction, so that to explain the observed changes in emission energy we must have a well thickness that is increasing along the $(00\bar{1})$ direction. This change of well thickness has been confirmed through the x-ray data, but is not shown here.

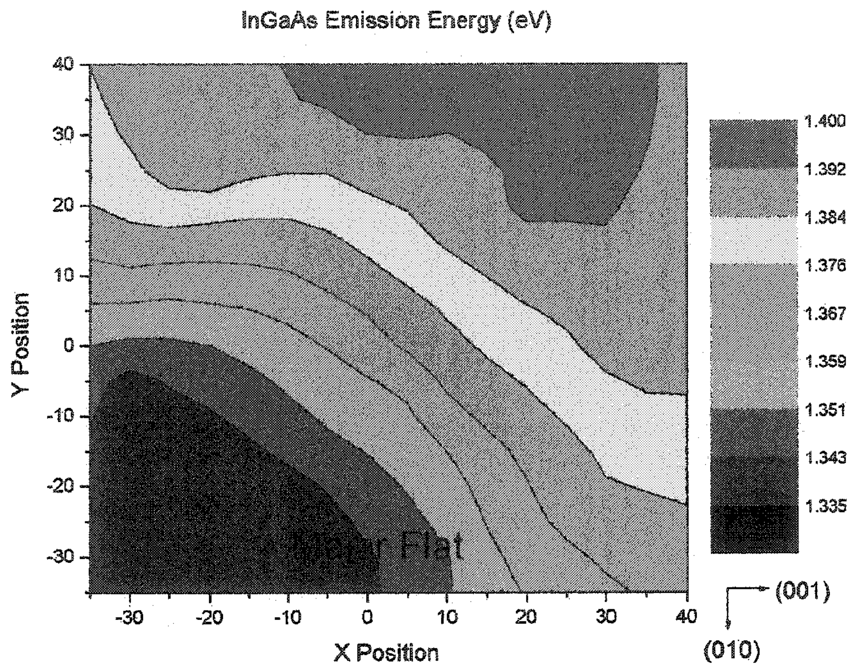

Fig. 5.10: Variation of InGaAs peak energy across the wafer.
Position in mm.

Figure 5.11 shows the variation of the InGaNAs peak energy with position across the wafer. The general trend observed is that the emission energy decreases from top to bottom of the wafer along the (010) direction, although at higher nitrogen content (i.e. towards the bottom of Fig 5.11), the presence of nitrogen related states in the bandgap complicates the interpretation of the photoluminescence and leads to a complicated energy map. This trend in the emission energy corresponds well to the variation in nitrogen concentration observed in Fig 5.6 above, without the added complications due to well width variations, because of the relatively wide InGaAsN well width.

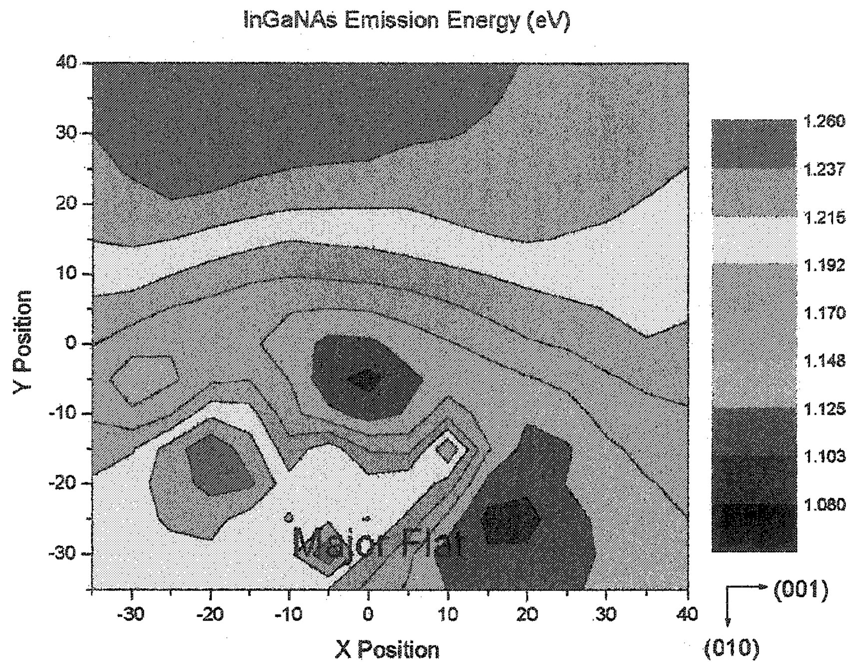

Fig. 5.11: Variation of InGaAsN peak position across the wafer.
Position in mm

5.3 Annealing of InGaNAs

Rapid thermal annealing experiments were performed on the InGaAsN material to determine if improvements in photoluminescence efficiency were produced in the same manner that was observed for GaAsN [6,7].

Figure 5.12 shows photoluminescence from the InGaAsN sample MBE2565 as a function of annealing temperature for a series of 60 second anneals. The as-grown sample was found to emit at approximately 1.08eV, whilst anneals at temperatures between 625°C and 850°C were found to progressively blue shift the luminescence, so that the emission energy reached approximately 1.145eV at an anneal temperature of 850°C.

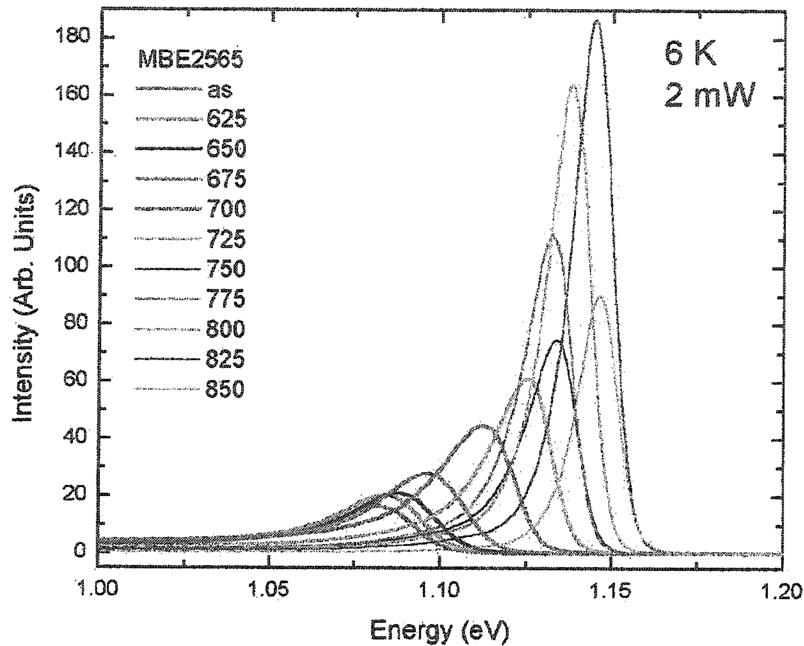

Fig. 5.12: Effect of rapid thermal annealing on the photoluminescence of MBE InGaAsN sample 2565. Measurements were taken at 6K using 2mW of HeNe excitation.

Accompanying the blue shift of the emission energy, we observe a large increase in the integrated emission intensity, along with a reduction in the full width at half maximum (FWHM) of the emission peak. The data is summarised in Fig 5.13 below. The improvement in the integrated intensity of the photoluminescence is found to increase monotonically by a factor of approximately three up to an anneal temperature of 825°C and then to decrease again for an anneal at 850°C. Even at 850°C however, the luminescence intensity is greater than for the as-grown sample. Accompanying the increase in luminescence yield, we observe a monotonic decrease in the FWHM, by approximately a factor of three up to the highest anneal temperature investigated.

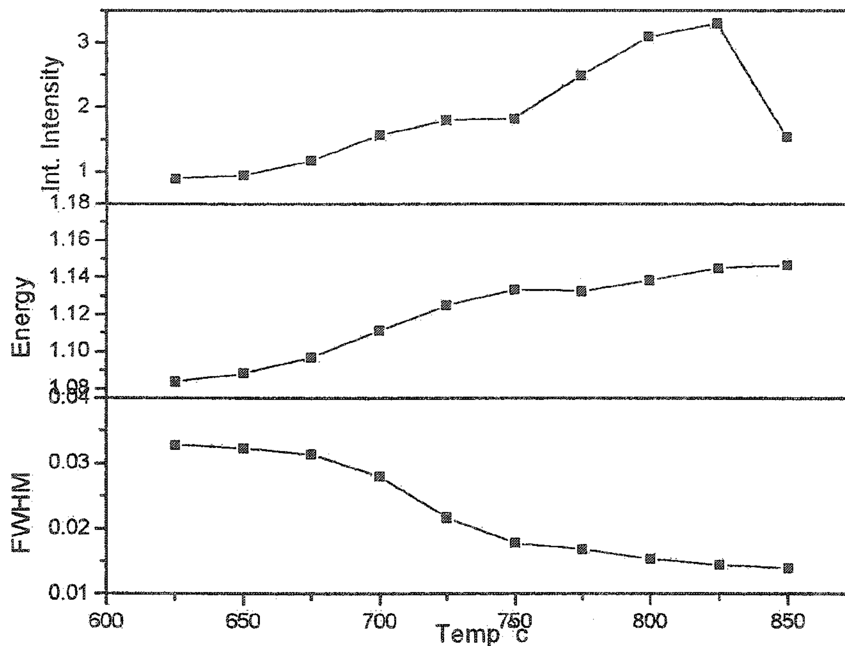

Fig. 5.13: Variation of integrated intensity, emission energy and full width at half maximum (FWHM) for MBE InGaAsN sample 2565.

As mentioned previously, the blue shift that is observed in these annealing experiments is not surprising, certainly at the higher temperatures, and could be accounted for by defects incorporated during crystal growth moving through the InGaAsN quantum well during annealing and causing intermixing between the well and barrier material. Such effects have certainly been observed previously for InGaAs materials [8,9,10]. Alternatively, the blue shift may be inherent to nitrogen containing quaternary material and result from a re-distribution of the nitrogen bonding configuration as suggested by Klar and co-workers [2] and seen by Kurtz et al. in vibrational experiments [1].

5.4 Temperature Dependent Measurements

To further understand the behaviour of InGaAsN material, photoluminescence measurements were taken as a function of sample temperature on an MBE sample annealed at various different temperatures. The annealing characteristics of the sample are shown below in Fig 5.14.

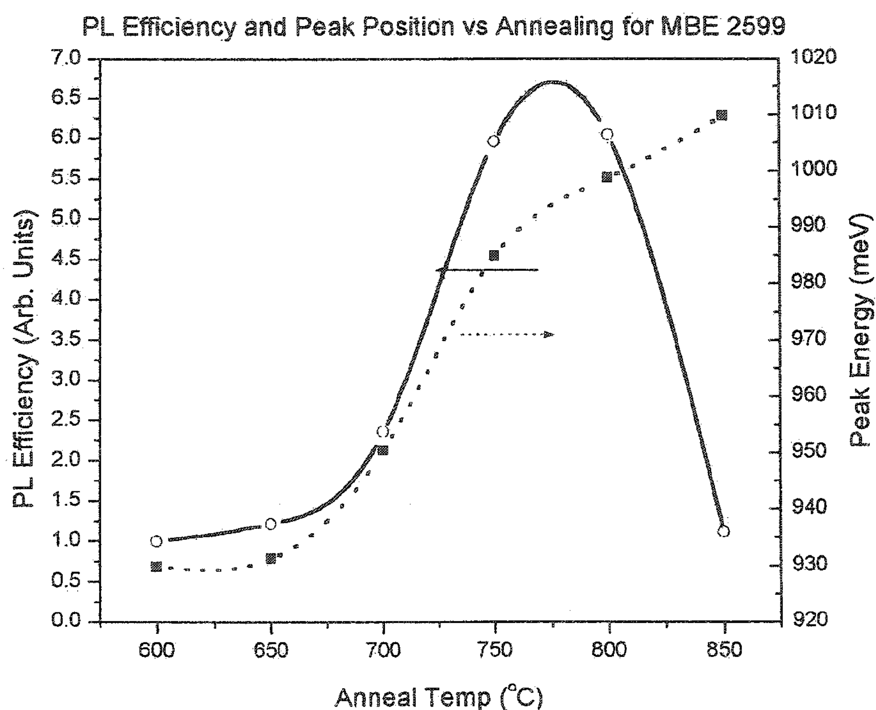

Fig. 5.14: Annealing characteristics of a single quantum well InGaAsN sample. Efficiency corresponds to the ratio of integrated intensity to that at 600°C

Behaviour similar to that described in section 5.3 above, including an increase in the luminescence intensity and a strong blue shift, are again observed as a function of increasing anneal temperature. The photoluminescence intensity as a function of the sample temperature is shown for this same sample in Fig 5.15 below.

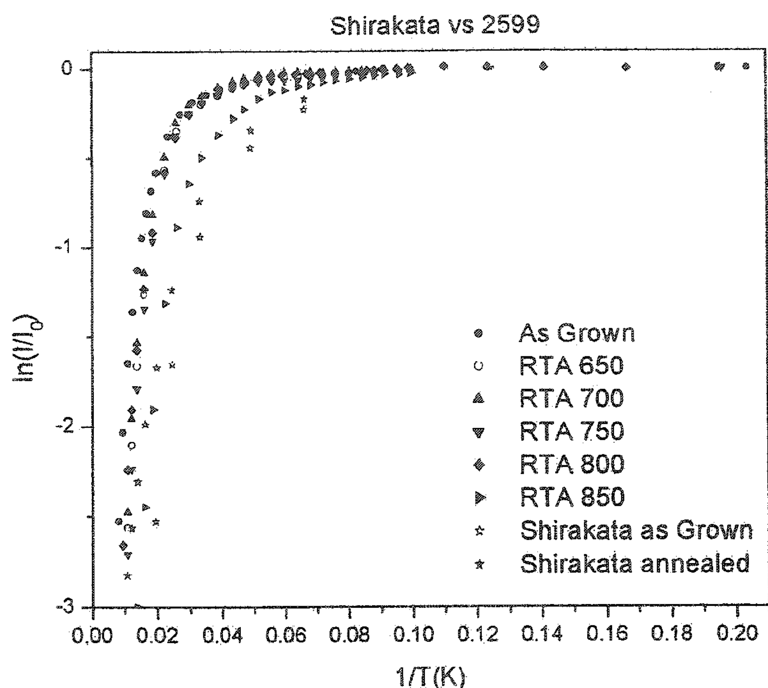

Fig. 5.15: Variation of integrated luminescence intensity with sample temperature for MBE2599.

Note that the integrated intensity data as displayed, is scaled to I_o, the integrated intensity at low temperature, and that the large changes in absolute intensity as a function of annealing conditions are therefore not apparent. Figure 5.15 also includes data extracted from a paper by Shirakata and co-workers [11], who investigate an InGaAsN sample similar to that described here. As a function of increasing sample temperature, the integrated intensity is observed in fig 5.15 to remain initially constant and then to decrease strongly, beginning at a temperature that depends upon the annealing conditions [12].

For non-nitrogen-containing, InGaAs samples grown under non-ideal conditions, such as the low growth temperatures employed for the InGaAsN samples discussed here, a variety of point-defect structures are expected to be incorporated. At low growth

temperatures Arsenic anti-site defects are common for example, which correspond to an Arsenic atom residing on the Gallium site of the lattice. As mentioned in chapter 3, such defects act as efficient trapping sites for excitons, immobilizing them at low temperature and helping to isolate them from non-radiative sites that would otherwise be accessible to the mobile excitons. If such traps are present in the InGaAsN samples, then as the samples are warmed up from the low temperature regime in which all excitons are trapped, we expect to observe a loss in luminescence intensity, as non-radiative sites become accessible.

As a function of sample temperature, we can write the number of trapped excitons, N(T), as,

$$N(T) \sim \frac{1}{1 + C.T.e^{-E_b/KT}}$$

where E_b is the binding energy of the exciton to the trap, K is Boltzmans constant and C is a constant related to the number of binding sites [13,14,15]. For a number of binding sites N_s, we have,

$$C = \frac{2\pi MK}{N_s h^2}$$

where M is the exciton mass and h is Plancks constant.

If we assume that the integrated photoluminescence intensity is proportional to the number of trapped excitons, we can use the data as a function of sample temperature to extract the number of trap sites for a given exciton binding energy. In principle we can use fits to the temperature data to extract both a trap density and a binding energy, but in

practice we find that the fit to the experimental data is somewhat insensitive to the binding energy, so that instead we choose to calculate the trap density for a variety of assumed binding energies. Trap densities extracted in this way, as a function of sample annealing conditions, are shown below in Fig 5.16,

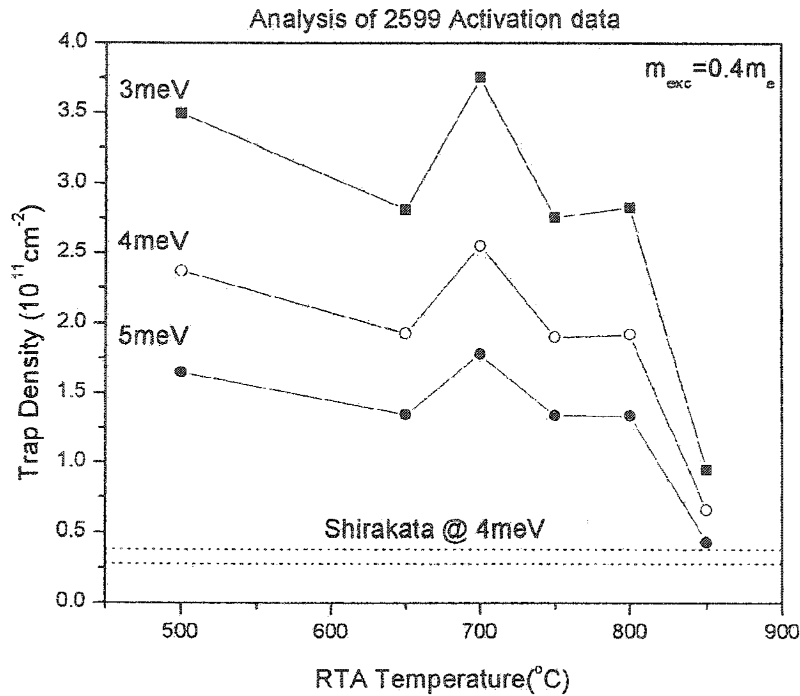

Fig. 5.16: Trap density as a function of sample anneal temperature for InGaAsN sample MBE2599.

Also shown in Fig 5.16 is the trap density extracted from a fit to the data of Shirakata and co-workers assuming an activation energy of 4meV.

From Fig 5.16 we see that the general trend in the data is of a decreasing trap density as a function of increasing anneal temperature, independent of the exact value chosen for the exciton binding energy. The data of Shirakata and co-workers can be explained as being similar to our own, but for a somewhat smaller trap density. However,

it is clear that the present model cannot fully explain the observed variation of PL emission efficiency with changing anneal conditions, because improvements in luminescence efficiency are present even at low temperatures, where all excitons should be bound within the model presented here. Such behaviour requires the presence of a non-radiative recombination pathway that is reduced during annealing.

5.5 Conclusion

In this chapter we have investigated the optical properties of quaternary InGaNAs material grown by both MOCVD and MBE. The material grown by both techniques is found to display photoluminescence that can be strongly enhanced by the use of rapid thermal annealing techniques. Such annealing is found to produce strong increases in the luminescence efficiency and associated reductions in the emission line width, but is accompanied by strong blue shifts of the emission energy. Measurements across a complete InGaAsN MBE wafer have been used to determine appropriate conditions for future growths. Photoluminescence measurements as a function of sample temperature have shown behaviour that can be interpreted in terms of defects incorporated during growth, although the presence of a non-radiative pathway is needed to understand the results in detail.

References

[1] Steven Kurtz, J. F. Klem, A. A. Allerman, R. M. Sieg, C. H. Seager, and E. D. Jones, Appl. Phys. Lett. **80**, 1379 (2002).

[2] P. J. Klar, H. Gruning, J. Koch, S. Schafer, K. Volz, W. Stolz, W. Heimrodt, A. M. Kamal Saadi, A. Lindsay, and E. P. O'Reilly, Phys. Rev. B **64**, 121203(R) (2001).

[3] Sarah Kurtz, J. Webb, L. Gedvilas, D. Friedman, J. Geisz, J. Olson, R. King, D. Joslin, and N. Karam, Appl. Phys. Lett. **78**, 748 (2001).

[4] S. A. Choulis, T. J. C. Hosea, P. J. Klar, M. Hofmann, and W. Stolz, Appl. Phys. Lett. **79**, 4277 (2001).

[5] K. Kim and A. Zunger, Phys. Rev. Lett. **86**, 2609 (2001).

[6] H. P. Xin, K. L. Kavanagh, M. Kondow, and C. W. Tu, Journal of Crystal Growth **208**, 145 (2000).

[7] H. P. Xin, K. L. Kavanagh, M. Kondow, and C. W. Tu, Journal of Crystal Growth **201-202**, 419 (1999).

[8] E. H. Li, Ed., *Quantum Well Intermixing* for Photonics, SPIE Milestone Series 1, Bellingham, MA, 1998, **145**.

[9] J. H. Marsh, "Quantum well intermixing," *Semiconduct. Sci. Technol.*, vol. **8**, pp. 11361155, (1993).

[10] E. H. Li, Ed., *Semiconductor Quantum Well Intermixing-Material Properties and Optoelectronic Applications*. (Amsterdam, The Netherlands: Gordon & Breach, 1998).

[11] Sho Shirakata, M. Kondow, and T. Kitatani, App. Phys. Lett. **80**, 2087, (2002).

[12] A. Polimen, M Capizzi, M Geddo, M. Fischer, M. Reinhardt, and A. Forchel, Phys. Rev. B **63** (2001).

[13] J. D. Lambkin, D. J. Dunstan, K. P Homewood, L. K. Howard, and M. T. Emeny, App. Phys. Lett. 57 1986 (1990).

[14] G. Bacher, C. Hartmann, H. Schwiezer, T. Held, G. Mahler, and H. Nickel, Phys. Rev. B **47**, 9545 (1993).

[15] J. E. Zucker, A. Pinczuck, D. S. Chemla, and A. G Gossard, Phys. Rev. b 35, 2892 (1987).

Chapter 6

InGaNAs Laser Material

Following the optical characterisation of the InGaAsN material discussed in previous chapters, an attempt was made to fabricate a broad area InGaAsN diode laser operating at telecom wavelengths. In this chapter we discuss the laser that was designed and the processes that were used in its characterization.

6.1 Introduction

The InGaAsN materials system provides an opportunity to access the technologically important wavelength region around 1.3μm whilst remaining lattice matched to a GaAs substrate [1]. Since the introduction of these dilute nitride materials, a number of laser structures have been reported using various combinations of strained, unstrained and strain-compensated barrier materials [2-10]. For the laser structure discussed in this chapter, a single InGaAsN quantum well is chosen to provide gain with GaAsN barriers designed to tailor the emission wavelength to approximately 1.3μm, as discussed below [11].

6.2 Laser and Test Structure Design

The laser structure itself and two test structures designed specifically for photoluminescence optimization were grown by MBE in the modified VG V80H system discussed in previous chapters. The two samples grown for PL characterisation consisted of 7nm $In_{0.33}Ga_{0.67}N_{0.02}As_{0.98}$ single quantum wells with either GaAs barriers (sample A) or 10nm $GaN_{0.03}As_{0.97}$ barriers (sample B). Both samples were grown on (001) semi-insulating GaAs substrates, with the quantum well and barrier regions grown at 450°C and GaAs and 90nm GaAs cap regions grown at 600°C. A Schematic of the band alignment in the two samples is shown below in fig. 6.1.

The laser structure itself was grown on an n^+-GaAs substrate and consisted of two1.5μm thick $Al_{0.33}Ga_{0.67}As$ cladding regions on either side of the nitrogen containing active region. This active region consisted of a single 7nm $In_{0.33}Ga_{0.67}N_{0.02}As_{0.98}$ quantum well

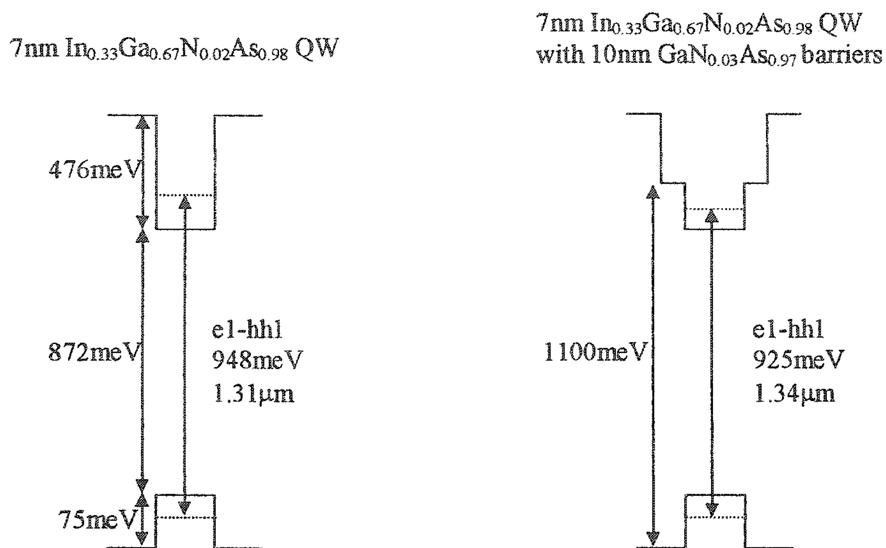

Figure 6.1 Schematic diagram showing the band alignment for the two samples used in photoluminescence characterization.

with 10nm $GaN_{0.03}As_{0.97}$ barriers placed at the center of a 30nm GaAs spacer. For current injection, the top $Al_{0.33}Ga_{0.67}As$ cladding layer was p-doped with Beryllium at $5x10^{17}cm^{-3}$ whilst the bottom cladding layer, closest to the substrate, was n-doped with Silicon at $1x10^{18}cm^{-3}$ and separated from the substrate by a GaAs buffer layer doped at $2x10^{18}cm^{-3}$. For contacting, the structure was capped with 200nm of GaAs doped with Beryllium at $1x10^{19}cm^{-3}$. A schematic of the laser layer structure is shown in fig. 6.2.

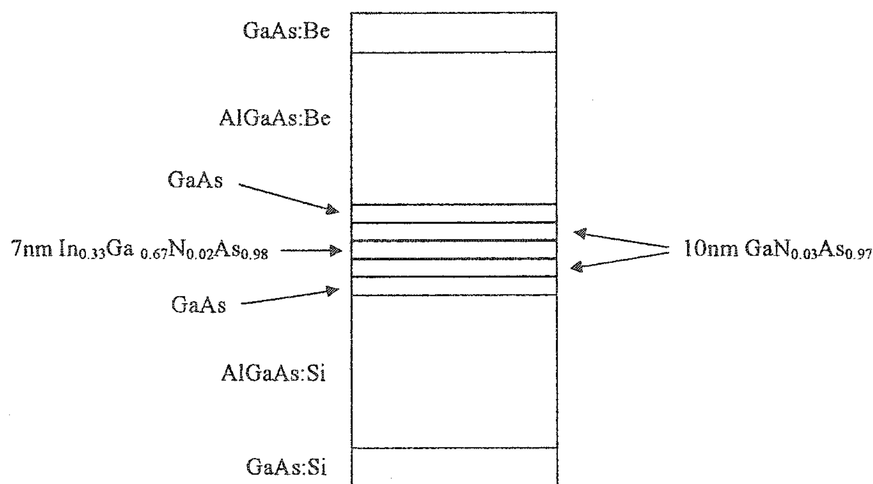

Figure 6.2 Layer structure of the InGaNAs diode laser

For testing, broad area devices of width 40μm were prepared using chemically assisted ion beam etching (CAIBE). Contacts were deposited using Ti-Pt-Au and Au-Ge-Ni combinations for the p- and n-type contacts respectively. Uncoated Fabry-Perot cavities were prepared in various lengths by back thinning and cleaving and the finished devices were placed p-side up onto copper heat sinks.

6.3 Optical Characterization

For rapid thermal annealing experiments, samples A and B were each cleaved into a number of pieces and subject to anneals for 60 seconds at a number of temperatures i.e. each piece was annealed at only one temperature. A summary of the room temperature

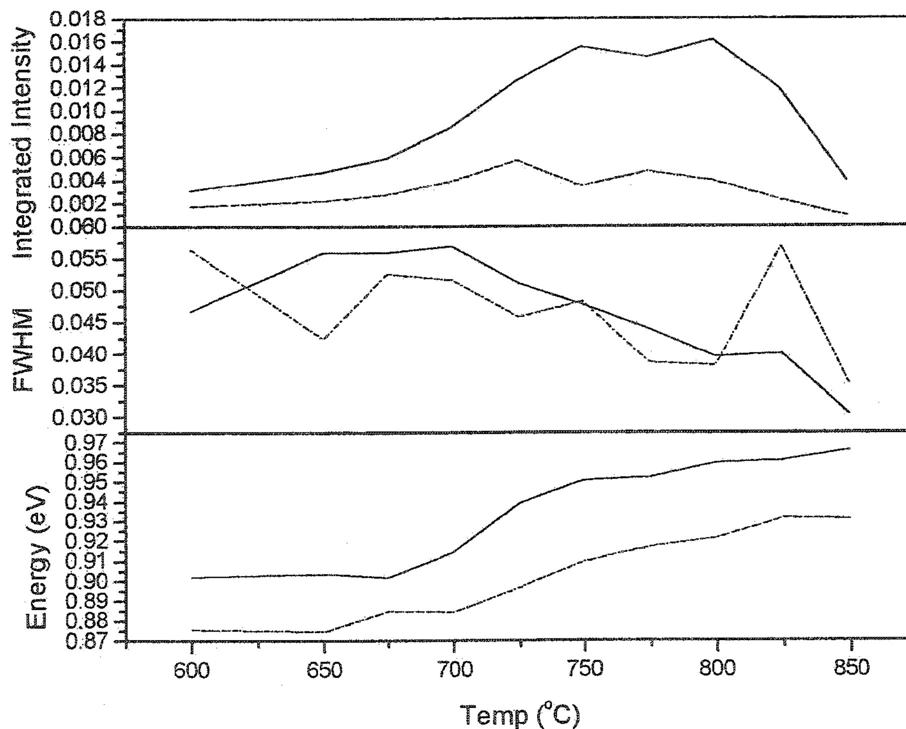

Figure 6.3: Effect of rapid thermal annealing on the integrated PL intensity, the full width and the emission energy for samples A (solid) and B (dashed) discussed in the text.

photoluminescence data is given in fig. 6.3. As has been discussed in previous chapters, the rapid thermal annealing treatment produces a blue shift of the emission energy with increasing temperature, a reduction in the full width at half maximum and an increase in the photoluminescence intensity which peaks at approximately 750-800°C. Above about 800°C, the PL intensity begins to decrease as a function of increasing anneal temperature. In comparing the behavior of the two samples we see that sample B, with $GaN_{0.03}As_{0.97}$ barriers, produces a consistently lower transition energy than sample A under all annealing conditions. The difference in transition energies varies between approximately 25meV and 40meV across the annealing temperature range and can be directly associated with the reduction in quantum confinement in sample B that results from a reduction in the barrier height.

6.4 Laser Tests

Structures of type B, discussed above, were processed further, after annealing at 800°C, to produce broad area laser structures. These structures were then electrically contacted and both their electroluminescence spectrum and their light output vs. current characteristics were measured at room temperature by Dr. James Gupta at the NRC [12].

In fig. 6.4 below we show a typical electroluminescence spectrum taken above laser threshold. The output consists of a single peak at a wavelength of approximately 1.36 microns, with a full width at half maximum of approximately 6nm, limited by the spectral resolution of the grating spectrometer used in the measurements.

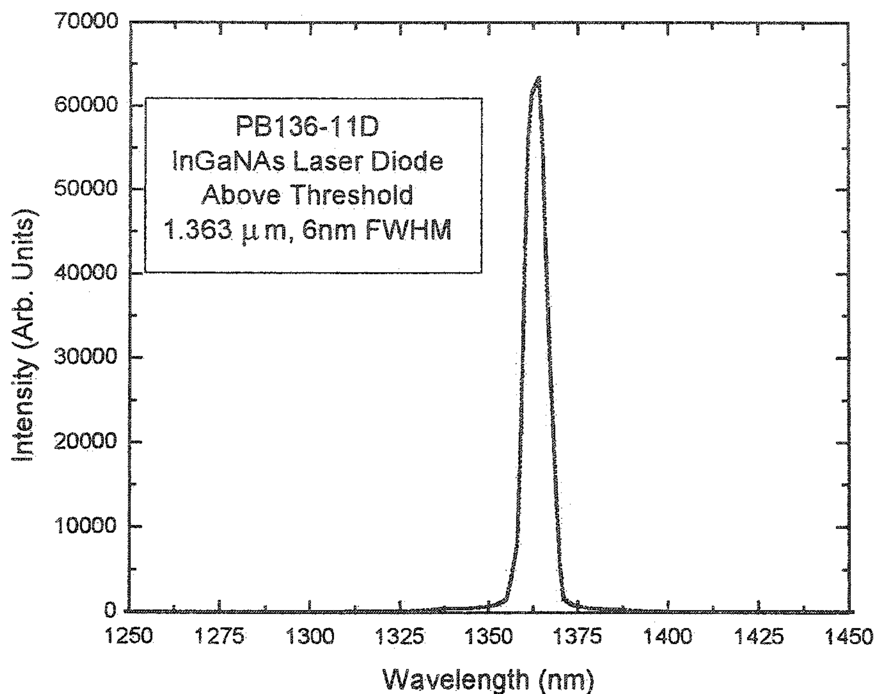

Fig. 6.4: Room temperature electroluminescence spectrum from the first InGaAsN laser to be grown at the NRC.

The light output from a typical device as a function of injected current density, i.e. current per unit contact area, is shown in Fig. 6.5. The threshold current density for this particular device is seen to be approximately 1250 Amps/cm^{-2}. Below this value, the light output is dominated by spontaneous emission. At threshold, the gain of the laser cavity, provided by the InGaAsN material itself, is just sufficient to overcome the losses within the cavity and stimulated emission begins to dominate. The loss mechanisms that must be overcome to allow lasing to begin include such effects as light emission from the cleaved end mirrors of the cavity, absorption losses within the semiconductor and scattering losses at the various interfaces within the device [9,13,14].

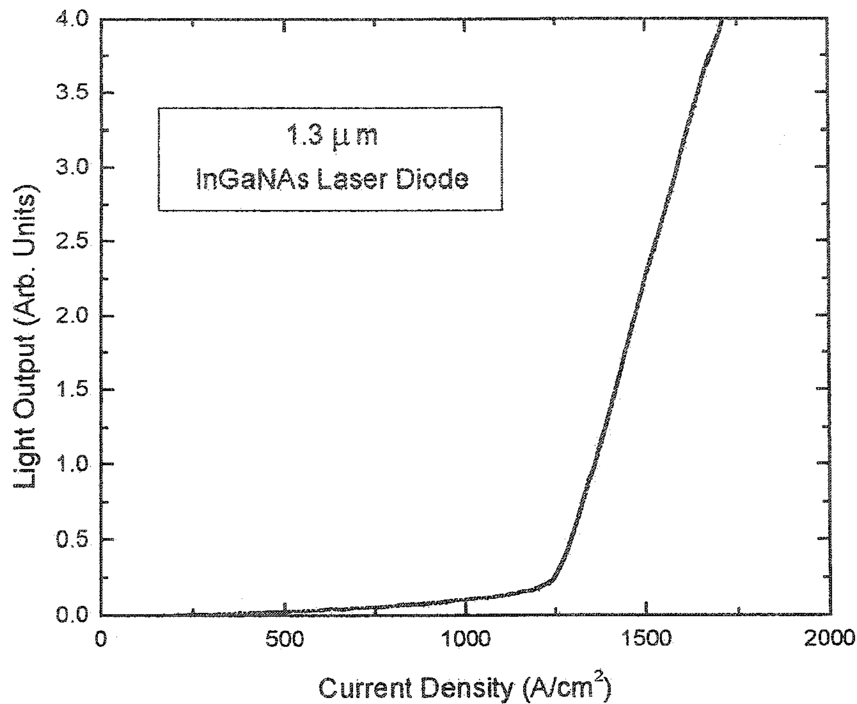

Fig 6.5: Room temperature light output vs injected current density for a typical InGaAsN laser fabricated from the NRC material.

By examining the variation of the light output vs current density, i.e. the device LI curve, for a series of devices with different cavity length, it is possible to extract values for the internal cavity losses and for the internal quantum efficiency of the recombination process. For this first set of NRC lasers, the internal quantum efficiency was found to be approximately 53%, whilst the distributed losses were approximately $10cm^{-1}$ [15].

6.5 Conclusions

In this chapter we have discussed the characterisation of the InGaAsN sample used in the first NRC, long wavelength laser and the preparation and testing of the finished broad area laser. Following the annealing techniques developed and described in

previous chapters, we have been successful in producing a working laser suitable for telecommunication applications around λ=1.3μm.

References

[1] M. Kondow, T. Kitatani, S. Nakatsuka, MC Larson, K. Nakahara, Y. Yazawa, et al. IEEE J Sel Top Quantum Electron, **3** (3), 719–30 (1997).

[2] T. Miyamoto, K. Takeuchi, F. Koyama, K. Iga, IEEE Photon Technol Lett, 9 (11), 1448-50 (1997).

[3] B. Borchert, AY Egorov, S. Illek, H. Riechert, IEEE Photon Technol Lett, **12** (6), 597–9 (2000).

[4] DE Mars, DI Babic, Y Kaneko, Y-L Chang, S. Subramanya, J. Kruger, et al. J Vac Sci Technol B, 17(3), 1272-5 (1999).

[5] DA Livshits, AY Egorov, H Riechert, Electron Lett, **36**(16), 1381–2 (2000).

[6] W. Li, T. Jouhti, CS Peng, J. Konttinen, P. Laukkanen, E-M Pavelescu, et al. Appl Phys Lett, **79**(21), 3386–8 (2001).

[7] SG Spruytte, MC Larson, W. Wampler, CW Coldren, HE Petersen, JS Harris Jr, J Cryst Growth, **227–228**, 506–15 (2001).

[8] AY Egorov, D. Bernklau, B. Borchert, S. Illek, D. Livshits, A. Rucki, et al, J Cryst Growth, **227–228**, 545–52 (2001).

[9] W. Ha, V. Gambin, M. Wistey, S. Bank, S. Kim, JS Harris Jr, IEEE Photon Technol Lett, **14**(5), 591–3 (2002).

[10] E. Tournie, M-A. Pinault, A. Guzman, Appl Phys Lett, **80**(22), 4148–50 (2002).

[11] E-M Pavelescu, CS Peng, T Jouhti, J. Konttinen, W. Li, M. Pessa, et al. Appl Phys Lett, **80**(17), 3054–6 (2002).

[12] J.A. Gupta , P.J. Barrios, G.C. Aers, R.L. Williams, J. Ramsey, Z.R. Wasilewski, Solid-State Electronics 47 399–405 (2003).

[13] M. Fischer, M. Reinhardt, A. Forchel. Electron Lett, **36**(14), 1208–9. (2000).

[14] M. Fischer, M. Reinhardt, A. Forchel, IEEE J Sel Top Quantum Electron 7(2), 149-51 (2001).

[15] Coldren LA, Corzine SW. Diode lasers and photonic integrated circuits. New York: John Wiley & Sons; 1995.

Chapter 7

Conclusions and Future work

This chapter discusses the conclusions that can be made from the work that has been presented in previous chapters and suggests further work that might be performed.

It is clear from the work presented in this thesis that it is possible to grow high quality GaAsN and InGaAsN material both by MBE and MOCVD. However, the introduction of nitrogen into both GaAs and InGaAs is challenging and further improvements in the growth procedures are necessary if the highest device quality material is to be achieved. The requirement of low growth temperature to allow nitrogen incorporation is particularly problematic and one would suspect that large improvement in sample quality and compositional uniformity would occur if the sample temperature could be raised whilst still maintaining efficient nitrogen incorporation.

Photoluminescence mapping of the InGaAsN bandgap has been accomplished and has been useful in optimizing the growth conditions for MBE material. No such measurements have been attempted for MOCVD material, partly because the uniformity cannot be easily altered simply by stopping sample rotation. For MOCVD material, the nitrogen composition and optical quality have been investigated as a function of growth conditions, including TBA flow and DMHY flow conditions. Nitrogen incorporation during MOCVD growth is found to depend only on the fraction of nitrogen in the gas phase, as evidenced both by x-ray measurements of concentration and by measurements of the optical bandgap.

Annealing studies have shown that substantial improvements in luminescence efficiency can be achieved but that bandgap blue shifting occurs at higher anneal temperatures. Annealing is found to improve both the luminescence intensity and the FWHM, although above approximately 750°C-800°C we observe a decrease in the luminescence efficiency or the development of defect related emission.

The mechanism for improvement of the luminescence efficiency during annealing is not clear and cannot be fully explained by the changes in trap density observed for InGaAsN material, given that changes in the luminescence intensity are observed even at low sample temperature, where excitons are expected to be fully bound. One possibility would be that there are non-radiative sites within the Böhr radius of the bound states, but this is yet to be determined experimentally. It is likely that time-resolved PL measurements would give us valuable information concerning the mechanism for improvement in the luminescence upon annealing, since one can then extract both radiative and non-radiative carrier lifetimes.

We have observed a large Stokes shift when comparing PL measurements with both PLE and absorption data. Such an effect could be caused by the clustering of nitrogen during growth, to produce large variation in the composition. In such cases, X-ray measurements give an average value of nitrogen concentration whereas the PL measurements will typically pick out the lowest energy gap. However, both absorption and PLE measurements are sensitive to the density of optically active states and should therefore give a more representative picture of the bandgap. A major problem with the PLE measurements is purely technical in origin and arises because of the difficulty in accessing a stable, CW, tunable laser that covers the complete wavelength range for the samples of interest. This problem does not arise for absorption measurements, where an incoherent, broadband source can be used, but these measurements have inherently lower signal to noise than the PLE measurements.

Future device work in the area of dilute nitride materials should focus on the design and growth optimization of long wavelength lasers. The preliminary results presented in chapter 6 are promising, but considerable improvement should be possible by careful optimization of growth parameters. One further area of laser study that could be pursued is that of vertical cavity surface emitting lasers. The present MBE system used for the growth of dilute nitrides includes an Aluminum effusion source, so that multi-layer GaAs/AlGaAs Bragg reflectors could be grown. Alternatively, multi-layer dielectric Bragg mirrors could be employed using the thin film dielectric deposition capabilities of the NRC.